The Great Deceiver: miR-2392's Hidden Role in Driving SARS-CoV-2 Infection

J. Tyson McDonald[1,2], Francisco Javier Enguita[1,3], Deanne Taylor[1,4,5], Robert J. Griffin[1,6], Waldemar Priebe[1,7], Mark R. Emmett[1,8], Marisa McGrath[9], Mohammad M. Sajadi[9], Anthony D. Harris[10], Jean Clement[9], Joseph M. Dybas[1,4], Nukhet Aykin-Burns[11], Joseph W. Guarnieri[1,12], Larry N. Singh[1,12], Peter Grabham[1,13], Stephen B. Baylin[1,14], Aliza Yousey[1,15], Andrea N. Pearson[15], Peter M. Corry[1,6], Amanda Saravia-Butler[1,16,17], Thomas R. Aunins[18], Prashant Nagpal[19,20,21], Cem Meydan[22,23], Jonathan Foox[22,23], Christopher Mozsary[22,23], Bianca Cerqueira[1,24,25], Viktorija Zaksas[1,26], Urminder Singh[1,27], Eve Syrkin Wurtele[1,27], Sylvain V. Costes[17], Diego Galeano[1,28,29], Alberto Paccanaro[1,28,30], Suzanne L. Meinig[31], Robert S. Hagan[31,32], Natalie M Bowman[33], UNC COVID-19 Pathobiology Consortium[34,35+], Matthew C. Wolfgang[31,35], Selin Altinok[36], Nicolae Sapoval[1,37], Todd J. Treangen[1,37], Matthew Frieman[1,9], Charles Vanderburg[38], Douglas C. Wallace[1,12], Jonathan Schisler[1,36], Christopher E. Mason[1,22,23,39,40], Anushree Chatterjee[1,18,19,20], Robert Meller[1,15], Afshin Beheshti[1,38,41,42,43*]

[1]COVID-19 International Research Team
[2]Department of Radiation Medicine, Georgetown University School of Medicine, Washington D.C. 20007, USA
[3]Instituto de Medicina Molecular João Lobo Antunes, Faculdade de Medicina, Universidade de Lisboa, Av. Prof. Egas Moniz, 1649-028 Lisbon, Portugal
[4]Department of Biomedical and Health Informatics, The Children's Hospital of Philadelphia, Philadelphia, PA 19104 USA
[5]Department of Pediatrics, Perelman School of Medicine, University of Pennsylvania, Philadelphia, PA 19104 USA
[6]Radiation Biology Division, Dept of Radiation Oncology, University of Arkansas for Medical Sciences, Little Rock, AK, 72211 USA
[7]Department of Experimental Therapeutics, University of Texas MD Anderson Cancer Center, Houston, TX, 77030, USA
[8]Department of Biochemistry and Molecular Biology, University of Texas Medical Branch, Galveston, TX 77555, USA
[9]Institute of Human Virology, University of Maryland School of Medicine, Baltimore, MD, 21201, USA
[10]Department of Epidemiology and Public Health, University of Maryland School of Medicine, Baltimore, MD, 21201, USA
[11]Division of Radiation Health, Department of Pharmaceutical Sciences, University of Arkansas for Medical Sciences, Little Rock, AK, 72211 USA
[12]Center for Mitochondrial and Epigenomic Medicine, Children's Hospital of Philadelphia, Philadelphia, PA 19104, USA
[13]Center for Radiological Research, Columbia University, New York, NY 10032, USA
[14]Department of Oncology, Sidney Kimmel Comprehensive Cancer Center, Johns Hopkins School of Medicine, Baltimore, MD 21287, USA
[15]Department of Neurobiology and Pharmacology, Morehouse School of Medicine, Atlanta, GA 30310, USA
[16]Logyx, LLC, Mountain View, CA 94043, USA

[17]Space Biosciences Division, NASA Ames Research Center, Moffett Field, CA 94035, USA

[18]Department of Chemical and Biological Engineering, University of Colorado Boulder, Boulder, CO, 80303, USA

[19]Sachi Bioworks Inc, Boulder, CO, 80301, USA

[20]Antimicrobial Regeneration Consortium, Boulder, CO, 80301, USA

[21]Quantum Biology Inc, Boulder, CO, 80301, USA

[22]Department of Physiology, Biophysics and Systems Biology, Weill Cornell Medicine, NY, 10065, USA

[23]The HRH Prince Alwaleed Bin Talal Bin Abdulaziz Alsaud Institute for Computational Biomedicine, Weill Cornell Medicine, NY, 10065, USA

[24]KBR Space & Science, San Antonio, TX, 78235, USA

[25]Aeromedical Neurology & Neuroimaging Research Group, United States Air Force School of Aerospace Medicine, Lackland AFB, TX, 78236, USA

[26]Center for Translational Data Science, University of Chicago, Chicago, IL, 60615, USA

[27]Bioinformatics and Computational Biology Program, Center for Metabolic Biology, Department of Genetics, Development and Cell Biology, Iowa State University, Ames, IA 50011, USA

[28]School of Applied Mathematics, Fundação Getulio Vargas, Rio de Janeiro, Brazil

[29]Faculty of Engineering, National University of Asuncion, Central, Paraguay

[30]Department of Computer Science, Centre for Systems and Synthetic Biology, Royal Holloway, University of London, Egham Hill, Egham, UK

[31]Marsico Lung Institute, University of North Carolina at Chapel Hill, Chapel Hill, NC, 27599, USA

[32]Division of Pulmonary Diseases and Critical Care Medicine, Department of Medicine, University of North Carolina, Chapel Hill, NC 27599, USA

[33]Division of Infectious Disease, School of Medicine, University of North Carolina, Chapel Hill, NC, 27599, USA

[34]Department of Oral and Craniofacial Health Sciences, UNC Adams School of Dentistry, University of North Carolina School of Medicine, Chapel Hill, NC, 27599, USA

[35]Department of Microbiology & Immunology, University of North Carolina School of Medicine, Chapel Hill, NC, 27599, USA

[36]McAllister Heart Institute, Department of Pharmacology, and Department of Pathology and Lab Medicine, The University of North Carolina at Chapel Hill, NC 27599, USA

[37]Department of Computer Science, Rice University, Houston, TX 77005, USA

[38]Stanley Center for Psychiatric Research, Broad Institute of MIT and Harvard, Cambridge, MA, 02142, USA

[39]New York Genome Center, NY, USA

[40]The Feil Family Brain and Mind Research Institute, Weill Cornell Medicine, NY, 10065, USA

[41]KBR, Space Biosciences Division, NASA Ames Research Center, Moffett Field, CA, 94035, USA

[42]Senior author

[43]Lead Contact

+The full list of authors associated with the UNC COVID-19 Pathobiology Consortium is available in the supplemental information.

88   *Correspondence: afshin.beheshti@nasa.gov

89

Summary (150 words)

MicroRNAs (miRNAs) are small non-coding RNAs involved in post-transcriptional gene regulation that have a major impact on many diseases and provides an exciting avenue towards antiviral therapeutics. From patient transcriptomic data, we have discovered a circulating miRNA, miR-2392, that is directly involved with SARS-CoV-2 machinery during host infection. Specifically, we found that miR-2392 was key in driving downstream suppression of mitochondrial gene expression, increasing inflammation, glycolysis, and hypoxia as well as promoting many symptoms associated with COVID-19 infection. We demonstrate miR-2392 is present in the blood and urine of COVID-19 patients tested, but not detected in COVID-19 negative patients. These findings indicate the potential for developing a novel, minimally invasive, COVID-19 detection method. Lastly, using both *in vitro* human and *in vivo* hamster models, we have developed a novel miRNA-based antiviral therapeutic targeting miR-2392 that significantly reduces SARS-CoV-2 viability and may potentially inhibit a COVID-19 disease state in the host.

Key words

COVID-19, SARS-CoV-2, microRNA, miRNA, Facile Accelerated Specific Therapeutic (FAST), FASTmer, miR-2392, antiviral therapeutic

Introduction

In Fall of 2019, the zoonotic spillover event led to the first know human infection with the severe acute respiratory syndrome coronavirus 2 (SARS-CoV-2) and subsequent human-to-human transmission triggered a pandemic leading to a worldwide health crisis from the resulting disease, referred to as coronavirus disease 2019 (COVID-19) (Huang et al., 2020; Zhu et al., 2020). COVID-19 causes substantial pulmonary disease but can also cause systemic health risks from extrapulmonary manifestations. Its effects entangle the entire body including but not limited to the cardiovascular, gastrointestinal, and hematological systems that may lead to long lasting effects after the virus has left the body, known as PASC (post-acute sequela of COVID-19) (Carfi et al., 2020; Feng et al., 2020; Gupta et al., 2020; Jacobs et al., 2020). SARS-CoV-2 is classified as a member of the Coronaviridae family, a group of viruses with a enveloped positive-stranded RNA that has the ability to infect cross-species (V'Kovski et al., 2021). Currently, three novel vaccines have completed efficacy trials and have been approved for emergency use by the Food and Drug Administration (Baden et al., 2021; Polack et al., 2020; Sadoff et al., 2021). While these vaccines represent a favorable milestone, additional data is required to demonstrate the long-term effectiveness against SARS-CoV-2 and protection against new strains. To prevent an endemic, the complete global eradication of COVID-19 will require a wide majority of the world's population to be vaccinated to achieve herd immunity. Unfortunately, there will always be a portion of the population that will not get vaccinated. Therefore, additional strategies for antiviral therapeutic options against COVID-19 are particularly relevant and important to explore in order to treat severe illnesses and overcome this global pandemic. Currently the majority of antivirals are repurposed drugs utilized for other disease and have shown limited clinical

131   efficacy, such as remdesivir (Abdelrahman et al., 2021). This brings a needed urgency to develop
132   antivirals specifically designed against SARS-CoV-2.

133   One potential avenue for an alternative antiviral agent is treatment against specific
134   microRNAs (miRNAs) associated with SARS-CoV-2 infection and subsequent manifestation of
135   COVID-19. MicroRNAs (miRNAs) are non-coding RNAs that are involved with regulation of
136   post-transcriptional gene expression and can impact entire pathways related to viruses and
137   diseases (Jiang et al., 2009; Trobaugh and Klimstra, 2017). Each miRNA can target multiple
138   messenger RNAs (mRNAs) and taken together, miRNAs are predicted to regulate over half of
139   the human transcriptome (Friedman et al., 2009). Recent evidence has shown different diseases,
140   including COVID-19, leads to distinct complements of miRNAs in the blood (Mishra et al.,
141   2020; Nersisyan et al., 2020; Portincasa et al., 2020; Sacar Demirci and Adan, 2020; Sardar et
142   al., 2020; Teodori et al., 2020; Widiasta et al., 2020; Zhang et al., 2021). These circulating
143   miRNAs are highly stable and have the potential to be used for minimally invasive novel
144   detection, potential biomarkers, and therapeutic targets (Tribolet et al., 2020). Research on the
145   interactions between miRNAs and viruses have revealed a multifaceted relationship.
146   Specifically, viruses have been shown to avoid the immune response by leveraging cellular
147   miRNAs to complete their replication cycle (Trobaugh and Klimstra, 2017). The following
148   mechanisms are central to the interaction of viruses and miRNAs: 1) miRNA processing
149   pathways can be blocked or inhibited by viruses interacting with key proteins such as Dicer and
150   associated proteins, 2) viruses can sequester miRNAs resulting in dysregulation of specific target
151   mRNAs, 3) viruses can utilize miRNAs to redirect regulatory pathways of other miRNA targets
152   to provide survival advantages, and 4) viruses can directly encode miRNA precursors that are
153   processed by the canonical miRNA cellular pathway and have well-defined functions to
154   specifically target and regulate the viral replicative cycle (Schult et al., 2018; Trobaugh and
155   Klimstra, 2017).

156   Here, we report on a miRNA, miR-2392, that may directly regulate and drive a COVID-19
157   response. This miRNA was initially predicted from COVID-19 patient data that consisted of
158   multiple miRNAs being suppressed/inhibited (miR-10, miR-10a-5p, miR-1-3p, miR-34a-5, miR-
159   30c-5p, miR-29b-3p, miR-155-5p, and miR-124-3p) and one miRNA being upregulated (miR-
160   2392). With further examination, we discovered miR-2392 to be a key miRNA involved with
161   COVID-19 progression. Specifically, miR-2392 drives downstream suppression of mitochondria
162   activity while increasing inflammation, glycolysis, and hypoxia. MiR-2392 upregulation was
163   concomitant with symptoms associated with COVID-19 infection in the host. We found that
164   miR-2392 was circulating in COVID-19 infected patients and increased as a function of viral
165   load. Our results demonstrate that miR-2392 may be utilized as an effective biomarker of
166   COVID-19. Furthermore, we have developed a miR-2392 inhibitor and provide evidence that its
167   use reduces SARS-COV-2 viability in targeted viral screens with A549 cells and reduces the
168   impact of infection in COVID-19 animal models. With further development this miR-2392
169   inhibitor may represent an effective antiviral therapeutic towards inhibiting the virus and limiting
170   a negative host response from COVID-19.

171

172   **Results**

173

174   *Identification of key miRNAs associated with COVID-19 infection*

175   Currently, the majority of the published literature associated with miRNAs and SARS-CoV-2
176 is based on *in silico* predictions. To identify miRNAs that may be involved in driving COVID-19
177 severity in the host, we first examined publicly available Bronchial Alveolar Lavage Fluid
178 (BALF) RNA-sequencing (RNA-seq) data from 13 individuals. Differential gene expression was
179 assessed using a 1.2-fold change in gene expression for p-values less than 0.01 revealing 42
180 increased genes and 347 decreased genes, compared to controls. Using the upstream regulator
181 analysis from the Ingenuity Pathway Analysis (IPA) knowledge database, the miRNAs from
182 differentially expressed genes (FDR < 0.05) from COVID-19-positive patients were inferred.
183 Eight miRNAs were predicted to drive significant changes in COVID-19 positive patients with
184 the downregulation of seven miRNAs (miR-10, miR-1, miR-34a-5p, miR-30c-5p, miR-29b-3p,
185 miR-124-3p, and miR-155-5p) and upregulation of a single miRNA, miR-2392 (**Fig. 1A**). Using
186 IPA's downstream effects analysis to predict biological processes from the combined
187 suppression of the seven miRNAs and the upregulation of miR-2392 resulted in increased
188 inflammation, immune suppression, and suppression of mitochondrial activity in the BALF
189 dataset (**Fig. 1B and 1C**).

190   In support of these findings, previous studies have shown alterations in specific miRNAs
191 may directly impact viral infections. For example, upregulation of miR-10, miR-124, or miR-1
192 have been shown to have antiviral roles during infection (Hu et al., 2020; Sardar et al., 2020;
193 Yang et al., 2016). Interestingly, upregulation of miR-30 and miR-155 have been shown
194 independently to provide suppression in other types of coronaviruses (Dickey et al., 2016; Ma et
195 al., 2018). The one miRNA predicted to be upregulated in COVID-19 patients from the BALF
196 data was miR-2392. Though limited, the existing literature on miR-2392 demonstrates it is
197 related to mitochondrial suppression and increased glycolysis (Fan et al., 2019) and circulating
198 factors related to negative health risks (Chen et al., 2013; Fan et al., 2019; Hou et al., 2019; Li et
199 al., 2017; Park et al., 2014; Yang et al., 2019).

200   Pathway analysis was performed with targets and pathways for miR-2392 to determine its
201 impact on the host when upregulated. We observed that the upregulation of miR-2392 in the
202 RNA-seq dataset impacted many downstream targets and pathways related to negative health
203 outcomes (**Fig. 1C**). In addition to mitochondrial suppression, we also predicted activation of
204 factors related to reactive oxygen species (ROS). Alternatively, since it is known that miR-2392
205 directly interacts with the mitochondrial DNA (mtDNA) to inhibit the levels of many of the
206 mtDNA coded oxidative phosphorylation transcripts, this could be a compensatory response to
207 the inhibition of mitochondrial bioenergetics.

208   Glycolytic pathways (**Fig. 1C**) are also upregulated in association with increased miR-2392.
209 MiR-2392 drives both hexokinase 2 (HK2) and pyruvate kinase (PKM) which are both positive
210 regulators of glycolysis. HK2 phosphorylates glucose to produce glucose-6-phosphate and is a
211 primary regulator of glycolysis. HK2 further enhances GDP-glucose biosynthesis. GDP-glucose
212 is a nucleotide sugar which an essential substrate for all glycosylation reactions (i.e.
213 glycosylation of viral spike proteins). Pyruvate kinase is essential for the production of ATP in
214 glycolysis as this enzyme catalyzes the transfer of the phosphate group from
215 phosphoenolpyruvate to ADP to make ATP. The mechanism of how miR-2392 is driving these

216 pathways is not clearly understood, but one possibility could be due to the stabilization of
217 glycolytic transcripts.

218   Overall, the miR-2392 observed upregulation of glycolysis and antiviral effects related to
219 miR-2392 suppression are consistent with the recently documented role of glucose metabolism in
220 the progression of viral infection and poor outcome of COVID-19 (Ardestani and Azizi, 2021). It
221 is also consistent with the reported effects of suppression of glycolysis by inhibitors like the
222 glucose analog, 2-deoxy-D-glucose (2-DG), that was shown to suppress SARS-CoV-2
223 replication in *in vitro* models (Ardestani and Azizi, 2021; Bojkova et al., 2020; Codo et al.,
224 2020). Interestingly, 2-DG is also 2-deoxy-D-mannose and as such can interfere with processes
225 utilizing mannose, a monosaccharide that is *in vivo* produced from glucose. Mannose plays
226 important roles in the glycosylation of specific proteins. Replacement of a mannose molecule by
227 2-DG in the respective SARS-CoV-2 N-glycans or O-glycans might lead to their truncation and
228 subsequently to the suppression of virus infectivity and proliferation. These and miR-2392 data
229 clearly indicate that selective targeting of glucose metabolism might have significant impact on
230 current and future SARS-CoV-2 pandemics.

231   Targets related to the goals of antioxidant N-acetyl cysteine (NAC) therapy are also observed
232 to be upregulated. These include activated endothelial cell increasing their expression of
233 numerous adhesion molecules, including intercellular adhesion molecule 1 (ICAM1), vascular
234 cell adhesion molecule 1 (VCAM1), and E-selectin, which allow attachment of hematopoietic
235 immune and non-immune cells to the endothelial surface, and thus, contribute to inflammation
236 and activation of the coagulation cascade. Powerful antioxidants such as NAC counteract
237 COVID19 infections by potentially suppressing viral replication via improving intracellular thiol
238 redox ratio as a precursor for major thiol antioxidant glutathione (Ho and Douglas, 1992) and
239 inhibiting the NF-kB pathway (Poppe et al., 2017). Inhibition of the NF-κB pathway has been
240 shown to reduce inflammatory damage by altering the glutathione and glutathione disulfide ratio
241 (Aykin-Burns et al., 2005; Griffin et al., 2003; Jia et al., 2010). Because NAC can also modulate
242 oxidative burst and reduce cytokine storm without weakening the phagocytizing function of
243 neutrophils (Allegra et al., 2002; Kharazmi et al., 1988; Sadowska et al., 2006), its use in
244 COVID-19 patients as a single agent or in combination with other antioxidants are being
245 conducted in clinical trials (Alamdari et al., 2020). A recent study has shown noteworthy
246 benefits of NAC in patients with severe COVID-19 infection (Ibrahim et al., 2020). Major
247 mechanisms proposed for these favorable patient outcomes were NAC's ability to reduce IL-6
248 induced mitochondrial oxidative stress via Complex I inhibition as well as to prevent increased
249 inflammation due to uncontrolled activation of mTORC1. These results were in line with the role
250 of miR-2392 in reducing the activities of electron transport chain complexes and enhancing
251 glycolysis, which is known to be induced by mTORC1 activation. The same study also
252 speculated that NAC could inhibit SARS-CoV-2 binding to ACE2 by reducing disulfide bonds in
253 its receptor-binding domain. Inflammatory pathways and others that are observed with COVID-
254 19 infection were also seen to be activated downstream of miR-2392.

255

256 *Conservation of miR-2392 between species and its predicted interactions with the SARS-CoV-2*
257 *genome*

258   Viral miRNAs can play a role in interspecies transmission due to the high conservation of
259   miRNAs among species and the ability of viruses to integrate miRNAs into its own genome
260   (Sacar Demirci and Adan, 2020; Schult et al., 2018). In addition, such integration of miRNAs
261   within the virus has been shown to assist viruses to replicate and evade the immune system
262   (Islam and Islam, 2021). To determine if miR-2392 might be capable of driving the observed
263   COVID-19 health risks and symptoms in the host, we analyzed the conservation of human miR-
264   2392 across species and the integration of miR-2392 into the SARS-CoV-2 genome (**Fig. 2**).

265   The UCSC Genome Browser was utilized to determine the conservation of miR-2392 across
266   different species (Kent et al., 2002). The mature 20 base-pair miR-2392 is derived from an 84
267   base-pair region of the 3´-UTR in the long non-coding RNA (lncRNA) gene, maternally
268   expressed 3 (MEG3) and located in an imprinted region DLK1-DIO3 that also contains three
269   clusters for the expression of 51 additional miRNAs (**Fig. 2A and 2B**). A base wise evolutionary
270   conservation comparison demonstrated that miR-2392 is highly conserved among non-human
271   primates. In addition, conservation of miR-2392 is evident in dogs, cats, and ferrets, species
272   known to be infected with SARS-CoV-2 while mice and rats, species not impacted by COVID-
273   19 (Johansen et al., 2020), have poor conservation with miR-2392.

274   To determine the impact of miR-2392 on normal tissues, we studied the impact of miR-
275   2392's host gene, MEG3, on normal tissues utilizing GTEx data (Consortium, 2020). For the
276   majority of healthy tissues, MEG3 was either not detected or being expressed at low levels (**Fig.
277   2B**). This can imply that miR-2392 does not seem to significantly affect normal tissues.

278   To explore potential binding sites for miR-2392, we used the miRanda software (Enright et
279   al., 2003) to identify all potential binding sites with respect to the SARS-CoV-2 reference
280   genome (Wuhan-Hu-1; NC045512.2) and representative genomes from lineages of concern. We
281   found that the miR-2392 seeding region is heavily integrated within SARS-CoV-2 and conserved
282   in different viral strains (**Fig. 2C**). The three best hits from the miRanda scores are located in the
283   NSP2, NSP3, and E-genes. Notably, these regions were conserved among 6 variants and lineages
284   of concern each represented by 14 recent genomes from the respective lineage available from the
285   Global Initiative on Sharing All Influenza Data (GISAID, (Shu and McCauley, 2017)).

286

287   *MiR-2392 targets mitochondrial and inflammatory pathways associated with SARS-CoV-2*

288   To determine in more detail the specific impact of miR-2392 gene targets and pathways in
289   COVID-19 patients, miR-2392 gene targets were retrieved from the miRmap database as
290   predicted by base pairing with its seed-region (Vejnar and Zdobnov, 2012). This list was further
291   refined by overlap found in several other miRNA databases including miRmap (Vejnar and
292   Zdobnov, 2012), miRwalk (Dweep and Gretz, 2015), miRDB (Chen and Wang, 2020), miRnet
293   (Chang et al., 2020b), and ClueGo (Bindea et al., 2009). We also included RNA-seq analysis of
294   39 autopsy tissue samples from the heart, lung, kidney, liver, and lymph node of COVID-19-
295   positive patients with high or low viral loads (Park et al., 2021). The refined list of miR-2392
296   gene targets (consisting of 375 genes) was examined using volcano plots in all samples (**Fig. 3A-
297   F**).

298   To better determine the systemic impact on miR-2392 gene targets in COVID-19, we
299   performed pathway analysis from the nasopharyngeal swab samples in living donors with and
300   without COVID-19 using the SARS-CoV-2 viral load as the independent variable (high,

7

301 medium, low, other virus). The miR-2392 gene targets are differentially expressed (FDR<0.05)
302 in at least one comparison of COVID-19-positive patients or other detected virus and were found
303 to separate into six distinct hierarchical clusters that were identified and annotated utilizing
304 ShinyGO (Ge et al., 2020) to determine the major pathways altered (**Fig. 3G**). The majority of
305 these upregulated miR-2392 targets are involved in immune and inflammatory pathways. The
306 downregulated miR-2392 targets were involved in mitochondrial function, oxidative stress, cell
307 cycle, developmental biology, and ubiquitin binding which are pathways recently associated with
308 the SARS-CoV-2 infection process (Hemmat et al., 2021). This data demonstrates miR-2392
309 may target several gene pathways related to perpetuating SARS-CoV-2 infection. For the
310 majority of the tissues (excluding the lymph nodes), higher viral loads are associated with greater
311 miR-2392 gene targets being regulated. Interestingly, the lymph nodes show an inverse
312 relationship with viral loads compared to other tissues.

313   Because miR-2392 was recently shown to directly target the transcription of mitochondrial
314 DNA genes (Fan et al., 2019), we evaluated the impact on expression of the mitochondrial miR-
315 2392 targets in our datasets. Differentially expressed miR-2392 target mitochondrial genes were
316 identified using the MitoCarta database (Rath et al., 2021) (**Fig. 3H**). This revealed 14 genes
317 harboring miR-2392 seed sequences that were significantly dysregulated in the nasal and heart
318 samples. In nasal samples, SLC25A28, mitoferrin which mediates mitochondrial iron transport,
319 was strongly upregulated along with IBA57, which is involved in iron sulfur assembly. The
320 mitochondrial outer membrane protein import complex subunit TOMM20, cytochrome c oxidase
321 (complex IV) subunit COX6B1, and mitochondrial transcription factor COT-2 (NR2F2) were
322 strongly down regulated. In the heart, the folate enzyme MTHFD2L (methylenetetrahydrofolate
323 dehydrogenase) was up-regulated while all of the other nuclear-coded mitochondrial genes
324 identified were down regulated. Downregulated heart mitochondrial genes included NDUFS5
325 (complex I subunit), COX6B1 and COX10 (complex IV structural and assembly subunits),
326 CKMT1A (mitochondrial creatine kinase), MRPL34 (subunit of the large subunit of the
327 mitochondrial ribosome), COT-2 (NR2F2), AK4 and MSRB3 (adenylate kinase 4 and
328 methionine-R-sulfoxide reductase which mitigate oxidative stress), MRS2 (magnesium
329 transporter) and CLIC4 (chloride channel). The kidney showed mild upregulation of complex I
330 and single methyl group metabolism, but down regulation of complex IV (COX10), regulatory
331 factor (COT-2), and iron sulfur center protein (IBA57). Hence, SARS-CoV-2 seems to
332 downregulate nuclear mitochondrial gene transcription in the more oxidative heart and kidney, as
333 well as in nasal tissues.

334   Since inflammation is a key component of COVID-19 infection, we also overlaid the
335 standard known inflammatory genes determined from Loza et al. (Loza et al., 2007) to the miR-
336 2392 targets (**Fig. 3I**). The analysis reveals that, at the mRNA level, most of the complement
337 pathway genes are upregulated in the tissue samples analyzed. These changes could be
338 compensatory, as proteins encoded by the genes could be downregulated as a function of
339 traditional miRNA effects. The responses reflect the importance of degrees of inflammation for
340 mediation of disease severity in COVID-19 patients and a key modulatory role of miR-2392 in
341 this context.

342   Proteomic and transcriptomic analysis on miR-2392 targets on blood from COVID patients
343 utilizing COVIDome (Sullivan et al., 2021) revealed interesting patterns between RNA and

344 protein levels for miR-2392 targets (**Fig. 3J and 3K**). We utilized the miR-2392 gene targets
345 only determined through miRmap to determine a broader relationship between the proteins and
346 genes. Several miR-2392 targets in the tissue show a significant transcription increase in
347 COVID-19-positive samples with small to no changes on the proteomics level: PLK1, CD38,
348 PYCR1, RNASE1, BIRC5, RRM2, SIGLEC1 (**Fig. 3J**). Interestingly, all these genes were also
349 positively regulated for the majority of tissues when considering only miR-2392 gene targets
350 with miRmap (**Figs. S1 and S2**). In the blood, the miR-2392 targets CXCL10, STAT1, IFIT3,
351 and C1QC were positively regulated at both the protein and gene levels. This upregulation was
352 also observed in all other tissues (**Figs. S1 and S2**). We explored the correlation between RNA
353 expression and protein abundance for miR-2392 targets in COVID-19 positive and negative
354 samples (**Fig. 3K**). Pearson correlation in both sample types is very close, with a slightly
355 stronger value in COVID-19 negative samples (negative samples cor=0.2089863, p-value=4e-10,
356 positive samples cor=0.2053345, p-value=8e-10). Further investigation is needed to understand
357 if increased levels of miR-2392 could potentially bind genes' mRNAs at a higher rate and
358 therefore prevent translation to protein or if there are other mechanisms preventing mRNA
359 translation to protein.
360
361 *Overexpression of miR-2392 simulates a phenotype similar to COVID-19 infection*
362 To determine if the upregulation of miR-2392 alone would elicit effects similar to a COVID-
363 19 infection, cells were treated with a miR-2392 mimic. Using RNA-seq data, there were 649
364 genes with a fold-change greater than ±1.2 and a p-value less than 0.05 (**Fig. 4A**). A number of
365 these differentially expressed genes were predicted targets of miR-2392 (**Fig. 4B**). Of particular
366 interest are differentially expressed genes in this model that are also dysregulated in SARS-CoV-
367 2 infected cells. We analyzed whole cell proteome data from a human-derived cell culture model
368 for a SARS-CoV-2 infection profile (Stukalov et al., 2021), and found 10 proteins that were
369 significantly changed in abundance and were also altered with miR-2392 overexpression: KIF22,
370 FKBP14, RAD51, AFAP1, ZCCHC17, ZWINT, MAGED1, CENPF, TMEM70, and NFKB2
371 (**Fig. 4C**). Viral infection is associated with alterations in protein posttranslational modifications
372 of cellular proteins, including ubiquitination. This phenomenon can occur by viral or host
373 directed modifications. We analyzed the ubiquitinome of the human-derived cell culture model
374 of SARS-CoV-2 infection and observed a number of proteins that were increased or decreased in
375 normalized ubiquitin abundance and were also dysregulated genes by miR-2392 overexpression.
376 Furthermore, we found miR-2392 overexpression impacted genes involved with mitochondria,
377 and inflammation (**Fig. 4D-4F**).
378 To determine if there was a direct correlation between miR-2392 overexpression and SARS-
379 CoV-2 infection, comparisons were made using gene expression fold-change values or overlap in
380 statically significant curated gene sets from canonical pathways determined by our fGSEA
381 analysis. Using previously published data from Blanco-Melo *et al.* (Blanco-Melo et al., 2020),
382 showed there was a statistically significant and positive correlation of the miR-2392 treatment
383 compared to both the A549 and Calu-3 cell culture models infected with SARS-CoV-2 (**Fig. 4G
384 and 4H**) as well as in lung biopsies post-mortem from two COVID-19 positive patients (**Fig.
385 4H**). Using nasal swab samples, a significant and positive correlation was determined between
386 patients with medium- and low-viral loads compared to non-infected patients (**Fig. 4I and 4J**).

9

387 Further identification of miR-2392 correlation to SARS-CoV-2 infections was made using RNA-
388 seq from multiple tissues (heart, kidney, liver, lymph node, and lung) obtained during autopsies
389 of COVID-19 patients with high or low viral loads (**Fig. 4I-J**). There was a positive correlation
390 to lung and lymph node tissues with miR-2392 expression. Interestingly, there was a significant
391 and positive correlation to liver tissue when comparing gene fold-change values (**Fig. 4I**) but not
392 fGSEA curated biological genesets (**Fig. 4J**). In contrast, a negative correlation to heart tissue
393 was observed.

394 Statistically significant pathways that were enriched due to miR-2392 treatment were
395 examined using fGSEA (**Fig. 4K-O**). It was observed that the miR-2392 treatment induced
396 pathway response that was significantly related to SARS-CoV-2 pathways. One obvious
397 relationship shows that the Reactome SARS-CoV-2 pathways were significantly activated for the
398 miR-2392 treated cells compared to the controls (**Fig. 4K and 4L**). Significant Hallmark
399 pathways (**Fig. 4N**) show distinct pathways that have been reported to be associated with
400 COVID-19 in patients, such as upregulation of hypoxia (Herrmann et al., 2020), glycolysis
401 (Ardestani and Azizi, 2021), and cell cycle pathways (Su et al., 2020). Interestingly, the KEGG
402 pathway analysis (**Fig. 4M**) indicates the overexpression of miR-2392 treated highly upregulated
403 systemic lupus erythematosus which has been reported to occur in COVID-19 patients and have
404 shown similar pathologies due to the increase of inflammation (Zamani et al., 2021).

405 Lastly, we determined the impact of miR-2392 specific targets being downregulated in the
406 cell lines after miR-2392 overexpression. A regulatory network was built by including the
407 predicted miR-2392 targets in the microRNA Data Integration Portal (MIRDIP) that were also
408 downregulated in the overexpression cell model as well as from the recently described consensus
409 transcriptional regulatory networks in coronavirus infected cells (Ochsner et al., 2020) (**Fig. 4P**).
410 The gene enrichment analysis of these putative miR-2392 targets showed the presence of GO-
411 terms related with the RNA metabolism, transcription, ribosome activity and Golgi complex
412 (**Fig. 4Q**).

413

414 *Circulating miR-2392 and the suppression of other miRNAs in COVID-19 infected patients*

415 To demonstrate the presence of circulating miR-2392 in COVID-19 infected patients, we
416 quantified the amount of miR-2392 by droplet digital PCR (ddPCR) in the serum, urine and
417 nasopharyngeal swab samples (**Fig. 5**). For the serum there were ten COVID-19 positive
418 intubated patients, ten COVID-19 positive patients (not intubated), and ten negative patients. For
419 the urine samples there were 15 inpatient COVID-19 positive samples, 15 outpatient COVID-19
420 positive samples, 10 inpatient COVID-19 negative samples, and 11 COVID-19 negative healthy
421 donors. Lastly, we quantified nasopharyngeal swab samples from 10 COVID-19 positive patient
422 samples, 6 common cold coronavirus positive patient samples (229E, HKU1, and OC43), and 6
423 Respiratory Illness/Coronavirus NL63 positive patient samples. In addition, we also quantified
424 three other miRNAs which we predicted to be inhibited by COVID-19 infection (**Fig. 1A**) which
425 were: miR-1-3p (**Fig. S3**), miR-155-5p (**Fig. S4**), and miR-124-3p (**Fig. S5**).

426 We observed a statistically significant increase of miR-2392 in COVID-19 positive patients
427 from both the serum and urine samples (**Fig. 5A**). In addition, Receiver Operating Characteristic
428 (ROC) curve analysis revealed that miR-2392 is significantly associated with SARS-CoV-2
429 infection in patients (**Fig. 5B**) in all tissues. Lastly, when dissecting the amounts of miR-2392

430   with specific conditions associated with infection, we observe that more severely affected
431   patients (i.e. intubated patients or patients in ICU), had higher presence of miR-2392 (**Fig. 5C**).
432   Interestingly, low levels miR-2392 appeared in the nasopharyngeal location with no significant
433   differences occurring between seasonal coronavirus samples. Since we hypothesize that miR-
434   2392 is a primary initiator for systemic impact of the infection, this might indicate that miR-2392
435   does not strongly appear until the virus has established its presence in the body.
436   As mentioned above we also measured the quantity of miR-1-3p (**Fig. S3**), miR-155-5p (**Fig.
437   S4**), and miR-124-3p (**Fig. S5**) and performed the same analysis. For miR-1-3p we observed
438   significant suppression in the serum while no significant differences in the urine or
439   nasopharyngeal samples (**Fig. S3**). MiR-1-3p is known to be beneficial for cardiovascular
440   functions, with the inhibition of miR-1-3p leading to heart failure and heart disease (Condorelli
441   et al., 2010). Similar response was observed for miR-155-5p with significant suppression in the
442   serum while no significant differences in the urine or nasopharyngeal samples (**Fig. S4**). For
443   miR-124-3p, we observed very low amounts (on average < 2 copies/5 ng RNA), for all
444   conditions, which indicates that miR-124-3p is not circulating for any of the patients for any the
445   conditions observed (**Fig. S5**). MiR-124-3p provides as an ideal miRNA negative control
446   candidate for SARS-COV-2.
447
448   *Inhibiting miR-2392: a novel antiviral COVID-19 therapeutic*
449   The link that we found between miR-2392 and COVID-19 infection prompted us to ask
450   whether we could develop effective antivirals for COVID-19 by inhibiting miR-2392. We used
451   the Facile Accelerated Specific Therapeutic (FAST) platform to develop an effective antisense-
452   based therapeutic against human miR-2392 (Aunins et al., 2020; Eller et al., 2021), termed
453   SBCov207, for the treatment of COVID-19 (**Fig. 6A**). The FAST platform combines the four
454   essential modules of drug development cycle (design, build, test, and learn) to optimize
455   therapeutics against any gene and species of interest in less than a week. The anti-miR-2392
456   FASTmer was evaluated for efficacy and toxicity against a SARS-CoV-2 infection of the human
457   lung cell line A549 (**Fig. 6B-D**). Treatment of uninfected A549 cells showed no cytotoxicity up
458   to 20 µM. The control nonsense FASTmer (SBCoV208) showed no toxicity even up to 40 µM.
459   Treatment of A549 cells infected with SARS-CoV2 showed drastic improvement in cell viability
460   with an average of 85% viral inhibition at 10 µM (IC50 of 1.15 ± 0.33 µM). In contrast, the
461   control nonsense FASTmer showed significantly lower viral suppression (**Fig. 6E-G**). Human
462   cell line-based infection models reaffirm that the anti-miR-2392 (SBCov207) is effective in
463   inhibiting SARS-CoV2, while not exhibiting toxicity at the concentrations tested.
464   In a separate *in vivo* model, the anti-miR-2392 FASTmer was evaluated in a Syrian hamster
465   infection model (**Fig. 6H-6J**). Initially six hamsters were treated with FASTmers for 72 hours
466   without infection to observe any changes in animal behavior indicating toxicity. There were no
467   observed changes in animal behavior indicating a lack of obvious toxicity. Following this study,
468   30 male hamsters were divided into 5 treatment groups. The infected hamsters were given 10^5
469   plaque forming units (pfu) of WA01/2020 strain of SARS-CoV-2 passaged twice in Vero E6
470   cells from the original isolate obtained from BEI Resources. The anti-miR-2392 FASTmer
471   treatment was given by intraperitoneal (IP) injection or intranasal (IN) instillation 24 hours
472   before viral inoculation or both 24 hours before and 24 hours after viral inoculation. Each

473 FASTmer dose was at a concentration of 10 µM in a 100 µL volume (approximately 0.13
474 mg/kg). Half of the hamsters in each group (n = 3) were euthanized and necropsied on day 3 and
475 7 post-infection respectively.

476   Loss of body weight of hamsters over the course of the experiment were <10% in all groups
477 and significantly different for the IN treatment one day before viral inoculation (compared to the
478 control) and while statistical differences between other groups were not present (**Fig. 6H**). Virus
479 titers from oropharyngeal swabs of hamsters receiving IN treatment were significantly lower ($p =$
480 0.018) than those from hamsters receiving FASTmers IP or PBS on day 1 post-challenge, but
481 there were no differences among groups in magnitude of shedding on days 2 and 3 post-
482 challenge (**Fig. 6I**). Although not statistically different than the control treatment, the data
483 indicates a downward trend with FASTmer treatment (**Fig. 6J**). In addition, the total
484 histopathological score for the IN was lower than the controls although not significant.

485

486 *The impact of miR-2392 on diseases, relationship to COVID-19 symptoms, and predicted FDA*
487 *drugs to target miR-2392*

488   To predict whether miR-2392 might have a direct relationship to COVID-19 symptoms in the
489 host, we determined the pathway and disease relevance of miR-2392 using miRnet (Chang et al.,
490 2020b). Among the diseases predicted to be associated with miR-2392 were a surprising number
491 of clinical observations present in individuals with COVID-19 infection (**Fig. 7A**). These include
492 heart or cardiovascular disease and failure, both known to heavily contribute to morbidity and
493 mortality in patients with COVID-19 (Nishiga et al., 2020), hyperesthesia (Krajewski et al.,
494 2021), as well as less common COVID-19 symptoms, such as lymphadenopathy and pharyngitis
495 related to sore throat (Edmonds et al., 2021; Walsh-Messinger et al., 2020), liver dysfunction
496 (Portincasa et al., 2020), splenomegaly (Malik et al., 2020), CNS (Mahajan and Mason, 2021;
497 Rodriguez et al., 2020) and kidney failure (Hultstrom et al., 2021).

498   It is interesting to note that miR-2392 was also predicted to affect diseases that appeared not
499 to be associated with COVID-19 infection, but literature searches reveal these pathologies do
500 occur in some COVID-19 patients. For example, azoospermia, which is linked to male infertility,
501 has been shown to occur in some male patients (Younis et al., 2020). The menstrual cycle in
502 females have been reported to be deregulated for months after COVID-19 infection (Li et al.,
503 2021). Association with dental damage has also been observed in COVID-19 patients (Sirin and
504 Ozcelik, 2021), also deafness or hearing loss (Koumpa et al., 2020). We used the tool Kaplan-
505 Meier Plotter (Nagy et al., 2018) to associate miR-2392 expression with pan-cancer patient
506 survival (**Fig. S7**). We observed that the high expression of miR-2392 is generally related to poor
507 prognosis with the majority of cancer types (p-value < 0.05). If miR-2392 is associated with
508 COVID-19, as we are hypothesizing, and is persistent after the virus clears the host, then the
509 implications for the potential long-term impact on the millions of people infected with COVID-
510 19 could be devastating. Intriguingly, one of the miR-2392 predicted consequences in the
511 immune category is decreased antibody levels in the blood; this might account for the reported
512 loss of the antibodies overtime (Gudbjartsson et al., 2020; Self et al., 2020).

513   Using computational prediction models, we also predicted small molecules, including FDA-
514 approved drugs that could inhibit miR-2392 from two different approaches. The first approach
515 employed a state-of-the-art machine learning method that we recently developed for predicting

516   missing drug targets (Galeano et al., 2021). We applied this algorithm on an association dataset
517   between 213 small molecules and 1,519 miRNAs from the SM2miR database (Liu et al., 2013)
518   (see statistics in **Fig. S8**). Our model also integrated chemical similarity between small
519   molecules and sequence similarity between miRNAs. In ten-fold cross-validation experiments,
520   we achieved an average area under the receiver operating curve of 0.877 when predicting
521   missing small molecule-miRNA associations (**Fig. S9**). A list of the top-20 predicted small
522   molecules for miR-2392 (**Fig. 7B**) includes Dexamethasone, the first drug known to save lives in
523   critically ill COVID-19 patients (Ledford, 2020), and Atorvastatin, that has shown similar
524   protective role in COVID-19 patients (Rossi et al., 2020). The second approach follows ideas
525   first presented in Sirota *et al.* (Sirota et al., 2011)and consists on analyzing the genomic signature
526   of miR-2392 (*i.e.* significant up and down-regulated genes) and predicting small molecules that
527   can reverse it. We screened the genomic signature of miR-2392 against the genomic signature of
528   30,000 small molecules contained in the connectivity map (CMAP) (Lamb et al., 2006). The top-
529   20 small molecules predicted by our approach (Sirota et al., 2011) includes the androgen receptor
530   antagonist Enzalutamide and the insulin sensitizer Pioglitazone (Carboni et al., 2020) both of
531   which are in clinical trials for COVID-19 (**Fig. 7C;** Clinical Trial #NCT04475601 and
532   NCT04604223). We also found literature evidence for the leukotriene inhibitor ubenimex (Asai
533   et al., 2020), and the bacterial DNA inhibitor metronidazole (Gharebaghi et al., 2020).

534

535   **Discussion**
536   While the potential eradication of the novel coronavirus through worldwide vaccination is
537   underway, there remains a major need to develop effective interventional strategies to minimize
538   the damage caused by coronavirus infections. Host-mediated lung inflammation is a driver of
539   mortality in COVID-19 critically ill patients. Thus, it is logical to focus on therapeutics that may
540   have immunomodulating properties or disrupt viral replication. Our research uncovers a novel
541   eight miRNA signature in patients with COVID-19 viral loads compared to those without disease
542   as predicted from RNA-seq data. The expression of seven miRNAs was decreased (miR-10,
543   miR-1, miR-34a-5p, miR-30c-5p, miR-29b-3p, miR-124-3p, and miR-155-5p) while a single
544   miRNA, miR-2392, was significantly increased (**Fig. 1**). This key miRNA signature was
545   involved in major cellular and molecular mechanisms that drives the viral-host response.
546   From previous research, the upregulation of miR-10a-5p, from the miR-10 precursor
547   miRNA, provides antiviral benefits through the suppression of SDC1 that can act as a defense
548   mechanism for Porcine hemagglutinating encephalomyelitis viruses (Hu et al., 2020). The
549   upregulation of miR-124 is shown to inhibit the Japanese encephalitis virus replication (Yang et
550   al., 2016). Notably, the upregulation of mir-30c-5p and miR-155-5p have been independently
551   shown to be involved with antiviral functions through immune and inflammatory pathways with
552   other type of coronaviruses (Dickey et al., 2016; Ma et al., 2018). It was also indicated that
553   inhibition of miR-34a-5p in the host by SARS-CoV-2 suppresses beneficial antiviral pathways
554   that this miRNA regulates. (Bartoszewski et al., 2020; Sacar Demirci and Adan, 2020). miR-1-3p
555   has previously been identified as an antiviral agent for viral related respiratory diseases and the
556   downregulation by SARS-CoV-2 is predicted to follow similar pathways for survival in the host
557   (Sardar et al., 2020). Examination of patients with COVID-19 showed increased levels of miR-
558   2392 circulating blood (**Fig. 5**). Interestingly, we show that for both miR-1-3p and miR-155-5p

559 from serum patient samples were significantly inhibited (**Figs. S3 and S4**), which is in
560 agreement with the current viral literature as discussed above. MiR-124-3p was shown to have
561 no significant changes and barely present for SARS-CoV-2 patients (**Fig. S5**), indicating the
562 responses discussed above is potentially specific for Japanese encephalitis virus.

563   Several studies have measured differential expression of miRNAs in COVID-19 patients and
564 proposed their use as biomarkers or therapeutics. A post-mortem examination from lung biopsies
565 in nine COVID-19 patients compared to controls found miR-26a, miR-29b, and miR-34a were
566 correlated to endothelial dysfunction and inflammatory biomarkers (Centa et al., 2020). In a
567 separate study performing multi-transcriptome sequencing in red blood cell depleted whole
568 blood from moderate or server COVID-19 patients four additional miRNAs, miR-146a, miR-21,
569 miR-142, and miR-15b, were identified as potential biomarkers as well as contributors to disease
570 pathogenesis (Tang et al., 2020). It has also been suggested to use miRNAs to target the
571 angiotensin-converting enzyme 2 (ACE2) receptor that facilities endocytosis of viral particles
572 into the cells to limit virus-induced glomerular injury, cell infection, kidney damage (Mishra et
573 al., 2020; Nersisyan et al., 2020; Pontecorvi et al., 2020; Sacar Demirci and Adan, 2020; Sardar
574 et al., 2020; Teodori et al., 2020; Widiasta et al., 2020). While these studies are limited to a
575 specific tissue, our data that correlates miRNA signatures from multiple tissues (**Fig. 3**) suggests
576 miR-2392 is a unique target that is ubiquitously involved in COVID-19 symptoms.

577   In 2010, miR-2392 was found in a small-RNA deep-sequencing of normal and malignant
578 human B-cells where it was altered among hundreds of other microRNAs (Jima et al., 2010).
579 Since then, the majority of publications with miR-2392 are focused on cancer tissues and have
580 found a potential role for miR-2392 in driving cellular invasion and metastasis through an
581 epithelial-mesenchymal transition. In 2013, miR-2392 was one of 6 circulating microRNAs
582 altered in the serum and tissue of patients with cervical squamous cell carcinoma that was used
583 to predict the occurrence of lymph node metastasis with the potential to assist in clinical staging
584 (Chen et al., 2013). Higher levels of miR-2392 in gastric cancer was found to be associated with
585 lower clinical staging and increased patient survival (Li et al., 2017). It was shown that miR-
586 2392 inhibited gastric cell invasion and metastasis by targeting MAML3 and WHSC1 for
587 degradation that subsequently decreased an epithelial-mesenchymal transition through the loss of
588 Snail1, Slug, and Twist1 expression. Similarly, miR-2392 and miR-1587 were found to target the
589 ZEB2 protein, a promoter of the epithelial-mesenchymal transition. A lower expression of these
590 two miRNAs were found in human keloid tissues that resulted in a loss of inhibition of ZEB2
591 and subsequent promotion of cellular proliferation and invasion in keloids (Hou et al., 2019).
592 Inhibition of miR-2392 by the long-non-coding RNA CACNA1G-AS1 was found to promote
593 hepatocellular carcinoma through disrupting the degradation of C1orf61, a tumor activator
594 associated with metastasis and tumor progression (Hu et al., 2013; Yang et al., 2019). Recently,
595 Fan et al. demonstrated a novel role for miR-2392 in the regulation of chemoresistance in tongue
596 squamous cell carcinoma by partial inhibition of mitochondrial DNA (mtDNA) transcription
597 through direct miRNA-mtDNA base pairing which resulted in reprogramming tumor cell
598 metabolism (Fan et al., 2019). These reports for miR-2392 establish the significant impact this
599 single miRNA may have in on cellular activity. Particularly relevant to this study was the altered
600 expression of miR-2392 found in Hepatitis B viral infections. Its expression was found to be
601 increased by more than 2-fold in extracellular vesicles secreted from human hepatocytes infected

14

with the Hepatitis B virus (Enomoto et al., 2017). While miR-2392 has a reported impact on tumor cell biology, our study expands the valuable therapeutic potential of targeting miR-2392 to subsequently decrease SARS-CoV-2 viral infections (**Fig. 6**). These results warrant further exploration of the mechanistic underpinnings for the role of miR-2392 in driving viral infection.

One therapeutic insight deduced from miR-2392 interactions is the importance of the mitochondrial oxidative phosphorylation (OXPHOS) and glycolytic pathways in COVID-19, dramatically highlighted in BALF samples reported in **Fig. 1C**. In a study of tongue squamous cell carcinoma (Fan et al., 2019) it was reported that miR-2392 enters the mitochondrion where it binds to Ago2 and then binds to nucleotides 4379 to 4401 in the mtDNA heavy (H) strand. This binding site is within the MT-TQ (tRNA glutamine) gene, which encompasses nucleotides m.4329-4400. MT-TQ is part of a large polycistronic transcript transcribed from the H-strand promoter. This transcript encompasses 12 of the mtDNA H strand polypeptide genes punctuated by tRNAs. Cleavage of the tRNAs releases the mRNAs. Up-stream of TM-TQ are the 12S and 16S rRNAs and the complex I gene MT-ND1 gene. Downstream of MT-TQ is MT-ND2, MT-CO1, MT-CO2, MT-ATP6/8, MT-ND3, MT-ND4L, MT-ND4, MT-ND5, and MT-CYB (Lott et al., 2013; Wallace, 2018). Strikingly, the down-regulated mtDNA genes from the BALFS are the complex IV (cytochrome c oxidase) genes MT-CO1 and MT-CO2, the complex III (the bc_1 complex) gene (MT-CYB), and the complex I genes (MT-ND2, MT-ND4, and MT-ND5) (**Fig. 1C** right side arc). Since the miR-2392 inhibition of mtDNA OXPHOS genes shown for the BALF samples (**Fig. 1C**) is also reflected in the miR-2392 down-regulation of the nuclear DNA coded mitochondrial transcripts of the complex I and IV genes and the iron-sulfur and heme iron complexes in the nasal, heart, and kidney autopsy samples (**Fig. 3D**), mitochondrial inhibition by miR-2392 appears to be the only physiological function that is common across all tissues in infected individuals. This suggests that mitochondrial modulation is a central feature of SARS-CoV-2 pathophysiology.

The inhibition of mitochondrial genes by miR-2392 would impair OXPHOS, which would have the most adverse effects on the high mitochondrial energetic tissues (brain, heart, kidney), the tissues central to the most severe COVID-19 cases. Inhibition of mitochondrial OXPHOS genes would increase mitochondrial reactive oxygen species (mROS) production, and induce glycolysis to compensate for the energy deficit (see top of **Fig 1C**). Mitochondrial function is regulated by the Sirtuins (Carrico et al., 2018), mitochondrial decline is associated with senescence, and mROS oxidation of mtDNA is linked to activation of the inflammasome and thus NFκB (West et al., 2015; West and Shadel, 2017; Zhong et al., 2018), all of which are modulated around miR-2392 (**Fig. 1C**). Thus, SARS-CoV-2 induction of miR-2392 (**Fig. 5**) and its associated inhibition of mtDNA and nuclear DNA OXPHOS genes (**Fig. 3** and **S1**) could explain many of the metabolic disturbances of COVID-19. Conversely, antagonism of miR-2392 function should ameliorate the inhibition of OXPHOS and may explain the therapeutic benefit of the anti-miR-2392 FASTmers.

Using miRNAs from serum as a biomarker was first established in patients for the examination of diffuse large B-cell lymphoma (Lawrie et al., 2008). The use of miRNAs as a diagnostic biomarker has several advantages. Circulating miRNAs are readily obtained through a minimally invasive blood draw and are remarkably resistant to degradation in the plasma and serum (Mitchell et al., 2008). Measuring differentially expressed miRNAs may also provide a

645 means to detect asymptomatic individuals as previously demonstrated in another viral infection
646 (Hou et al., 2017). However, potential confounding diseases that may influence the expression of
647 multiple miRNAs requires the further evaluation of the targets found in this study (**Fig. 5**).
648   Recent advances in RNA chemistry and delivery systems enabled the first miRNA-based
649 agents to enter into clinical trials several years ago (Rupaimoole and Slack, 2017). It was
650 discovered that miR-122 increased the stability and replication of the Hepatitis C virus (HCV)
651 through binding to the 5' end of the non-coding region that prevented degradation by the Xrn1
652 exoribonuclease (Jopling et al., 2005; Thibault et al., 2015). In a phase I clinical trial, a 15-
653 nucleotide phosphorothioate DNA–locked nucleic acid anti-miRNA that is designed to inhibit
654 miR-122 was first used and demonstrated no adverse reactions. In a subsequent phase IIa trial of
655 36 patients, there was a significant dose-dependent decrease in HCV load, one patient reported a
656 grade 3 adverse event (thrombocytopenia), and only a small set of patients experienced viral
657 rebound that may be linked to mutations of the HCV viral RNA (Janssen et al., 2013; Ottosen et
658 al., 2015). A separate clinical trial with a N-acetyl-Dgalactosamine (GalNAc)-conjugated anti-
659 miRNA targeting miR‑122 and antiviral agents (ledipasvir and sofosbuvir) was successful in
660 reducing viral loads in all treated patients within 4 weeks of treatment as well as sustained viral
661 response in three patients after 76 weeks of follow-up (van der Ree et al., 2017), however
662 subsequent treatments have been suspended due to two cases of severe jaundice. These clinical
663 trials have demonstrated the promising potential of using anti-miRNAs to significantly reduce
664 viral infection with limited adverse effects and the similarities with miR-2392 with SARS-CoV-2
665 warrant further investigations to push to clinical trials.
666   Presently, there remains no specific treatment option for patients presenting with severe
667 COVID-19 disease. While vaccines provide a promising avenue towards preventing the
668 development of these symptoms as well as curbing the infection rate, there remains an urgency to
669 successfully develop and implement therapeutic agents to reduce severe consequences from
670 infection and subsequent patient mortality. As the testing of antibody-based or drug targeted
671 therapies are currently underway, the added utility of miRNAs represents a novel category of
672 therapeutic agents that have previously shown endogenous activity to alter viral infection.
673

696   **Author contributions**
697   Conceptualization: A.B.; Methodology: A.B.; Formal Analysis: A.B., R.M., C.V., D.T., F.J.E.,
698   C.M., C.M., J.C.S., J.T.M., J.M.D., D.G., U.S., E.S.W., A.S., J.F., V.Z., N.S., T.J.T.;
699   Investigation: A.B., C.V., R.M., C.E.M., A.C., P.N., M.F., R.A.B., M.M., S.L.M., A.Y., T.R.A.;
700   Sample Collection: M.M.S., M.C.W., R.S.H., N.M.B., U.C.P.C., A.D.H., J.C.; Resources: A.B.,
701   R.M., C.E.M., A.C., M.S., M.F., M.C.W.; Writing – Original Draft: A.B., J.T.M.; Writing –
702   Review & Editing: A.B., J.T.M., F.J.E., R.J.G., W.P., M.M.S., J.M.D., J.W.G., D.W., S.B., V.Z.,
703   E.S.W., S.V.C., N.A, A.P., D.G., M.F., P.M.C., M.M., M.R.E., J.C.S., A.C., R.M., N.S., T.J.T.,
704   B.C., L.N.S., M.C.W.; Visualization: A.B., J.S.C, F.J.E, D.G., N.S., V.Z.; Supervision: A.B.;
705   Funding Acquisition: A.B.
706

707   **Declaration of Interests**
708   The authors declare no competing interests.
709

710   **Figure Legends**
711

712   **Figure 1. Key miRNA signature as predicted from Bronchial Alveolar Lavage Fluid
713   (BALF) RNA-seq data in patients with COVID-19. A)** Predicted upstream regulators
714   determined through Ingenuity Pathway Analysis (IPA) consistent with the transcriptional
715   response from differentially expressed genes (FDR<0.05; outer ring). Eight miRNAs were
716   among the key regulators in response to COVID-19 (inner ring). **B)** Major biological responses
717   resulting from dysregulation of this eight miRNA signature drive immune- and inflammatory-
718   related pathways as well as mitochondrial dysfunction determined through IPA. **C)** Pathway
719   regulation by miR-2392 from BALF RNA-seq data determined through IPA.
720

721   **Figure 2. Cross-species and viral integration of miR-2392. A)** The conservation of miR-2392
722   across species determined by UCSC Genome Browser. The boxes (■) represent aligning and
723   conserved sequence regions. Double horizontal line (=) represents both the genome and query
724   have unalignable sequence between regions of aligned sequence, a double-sided insertion. Single
725   lines (-) indicate gaps that are largely due to a deletion in the genome of the first species or an
726   insertion in the genome of the second species. **B)** The expression of MEG3, the miR-2392 host
727   gene, in different tissues from healthy patients. **C)** Potential binding sites of miR-2392 visualized
728   across 300 windows of 100bp length in SARS-CoV-2 genomes (NC045512.2 reference, and
729   representative genomes for variants and lineages of concern from GISAID). The score in each
730   window is the average of miRanda scores for hits within that 100bp window. Three top hits are
731   shown explicitly at the bottom of the plot.
732

733 **Figure 3. Gene targets of miR-2392 in COVID-19 patients as well as mitochondrial and**
734 **inflammatory genes.** Volcano plots showing the differential gene expression analysis from **A)**
735 nasopharyngeal swab and autopsy COVID-19 patient tissues from the **B)** heart, **C)** kidney, **D)**
736 liver, **E)** lung, and **F)** lymph node from RNA-seq datasets separated by viral load. **G)** Differential
737 gene expression analysis for all miR-2392 gene targets significantly expressed in nasopharyngeal
738 swab and autopsy COVID-19 patient tissues. The heatmaps display the t-score statistics for
739 comparing viral load vs negative patient sample for all samples. Main gene clusters were
740 determined through k-mean clustering. Six main gene clusters were determined and ShinyGO
741 (Ge et al., 2020) was utilized to determine the pathways for each cluster which are displayed on
742 the top panel of the heatmap. miR-2392 gene targets in for **H)** mitochondrial specific genes or **I)**
743 inflammatory genes are displayed. Differentially expressed genes are shown with at least one
744 comparison demonstrating a significant adjusted p-value (FDR<0.05) when comparing COVID-
745 19 patients (high, medium or low viral loads) to non-infected control patients (none). A heatmap
746 for the miR-2392 mitochondrial gene targets from the full list of targets determined only from
747 miRmap is available in **Fig. S1**. A heatmap for the miR-2392 inflammatory gene targets from the
748 full list of targets determined only from miRmap is available in **Fig. S2**. **J)** Scatter plot of $\log_2$-
749 transformed Fold Changes in RNAs and proteins for miR-2392 targets. The chart shows a set of
750 genes differentially expressed at the RNA level. Student's t-test, RNA p-value<= 0.05, no
751 limitation on protein p-value. **K)** Scatter plot of $\log_2$ transformed medians in RNAs and proteins.
752 The orange color represents COVID-19 positive samples, grey - COVID-19 negative samples.
753 Student's t-test is used in Fold Change calculations. The size and the opacity of the point
754 represent log2-transformed Fold Change at the RNA level. The shape of the point represents
755 Fold Change direction: circle - positive, triangle - negative. Pearson correlation for COVID-19
756 positive samples displayed in orange, for COVID-19 negative samples - in grey.

757

758 **Figure 4. Increased miR-2392 expression *in vitro* mimics a COVID-19 disease phenotype.**
759 **A-F)** Volcano plots for RNA-seq results in cells overexpressing miR-2392. **G-J)** Correlation plot
760 of RNA-seq between miR-2392 overexpression and related SARS-CoV-2 datasets. The circle
761 size is proportional to the correlation coefficient. Statistical significance was determined using a
762 two-tailed Student's t-test *p < 0.05, **p < 0.01, ***p < 0.001. **K-O)** Dot plots for statistically
763 significant gene sets determined by fGSEA. NES, nominal enrichment score. **P)** and **Q)**
764 Predicted miR-2392 targets by the MIRDIP algorithm that are downregulated in the
765 overexpression experiments. The putative miR-2392 mRNA targets belonging to the consensus
766 transcriptomic networks observed in SARS-CoV-2, MERS and Influenza infections of different
767 human cells are represented in a Venn diagram in the upper part of the panel **P**.

768

769 **Figure 5. Circulating miR-2392 with COVID-19 patients compared to COVID-19 negative**
770 **patients.** Droplet digital PCR (ddPCR) with specific primer for miR-2392 was performed on
771 serum, urine, and nasopharyngeal swab samples (including other seasonal coronavirus samples)
772 from COVID-19 positive and negative patients. The miRNA concentration is reported as
773 copies/5ng RNA. **A)** The levels of miRNA-2392 in all tissues from patients grouped as SARS-
774 CoV-2 positive (SARS-nCoV-2) or negative (neg). Unadjusted t-tests comparing the SARS-
775 CoV-2 positive to neg for each tissue are provided and also adjusted statistics comparing the

776 groups with a mixed model corrected for age and sex is provided. **B)** Receiver Operating
777 Characteristic (ROC) curve is provided for miR-2392 for each tissue comparing SARS-CoV-2
778 positive to negative patients. **C)** Comparing specific categories within each tissue type between
779 COVID-19 positive and negative patients. N = COVID-19 Negative, P = COVID-19 positive,
780 P_{int} = intubated patients, outp = outpatient, ICU = Intensive care unit/inpatient, Cold =
781 Coronaviruses related to the common cold, NL63 = NL63 coronavirus, and CoV-2 = SARS-
782 CoV-2. For all plots * = $p < 0.05$, ** = $p < 0.01$, and *** = $p < 0.001$. We also quantified three
783 other miRNAs with same patient samples as comparison which were miR-1-3p (**Fig. S3**), miR-
784 155-5p (**Fig. S4**), and miR-124-3p (**Fig. S5**).

785

786 **Figure 6. Anti-miR-2393 therapeutic mitigation of SARS-CoV-2 infection with *in vitro* and**
787 ***in vivo* models. A)** Schematic of the design for the miR-2392 inhibitor with the FASTmer
788 platform, the synthesis and formulation of the inhibitor, and the experimental models utilized for
789 testing the inhibitor. **B) – D)** Anti-miR-2392 FASTmer inhibitor applied to A549 human cells
790 infected with SARS-CoV-2 and tested for viral viability and cytotoxicity. Viral viability is
791 inhibited by 100% with near 0% cytotoxicity. **E) – G)** Nonsense FASTmer inhibitor applied to
792 A549 human cells infected with SARS-CoV-2 and tested for viral viability and cytotoxicity.
793 Viral viability is inhibited by 50% with near 0% cytotoxicity. **H) – J)** Toxicity and efficacy of
794 anti-miR-2392 FASTmer inhibitor in an *in vivo* infection hamster model. There were six
795 treatments groups: SBCov207 by IP injection 24 hours prior to viral inoculation (IP Day -1),
796 SBCov207 by IP injection 24 hours prior to viral inoculation and 24 hours post-viral challenge
797 (IP Day -1, +1), SBCov207 by IN injection 24 hours prior viral inoculation (IN Day -1),
798 SBCov207 by IN injection 24 hours prior viral inoculation and 24 hours post-viral challenge (IN
799 Day -1, +1), and 100ul of PBS as a control treatment 24 hours prior and post-viral challenge
800 through IN instillation (PBS IN Day -1, +1). **H)** Weights per day for each of the 5 groups pooled
801 (n = 6 for days 1 – 3 and n = 3 for days 4 -7), and the maximum percent weight loss, observing
802 for the two different endpoints. **I)** SARS-CoV-2 assayed by plaque assay on Vero E6 cells from
803 oropharyngeal swabs collected on days 1, 2 and 3. N=6 for each treatment group. **J)**
804 Histopathological total score for lung tissues at day 3; anti-miR-2392 treatments have lower
805 scores than the PBS control. Intranasal (IN), intraperitoneal (IP).

806

807 **Figure 7. Predicted impact of miR-2392 on human disease and the top-20 drug compounds**
808 **predicted to affect miR-2392 expression through machine learning approach**. **A)** Dot plot of
809 diseases associated with miR-2392, as predicted from miR-2392 gene targets by miRnet. The
810 diseases were manually curated to emphasize specific diseases and tissues. The values are plotted
811 according to p-value, and the size of each dot represents the number of downstream gene targets
812 for miR-2392 associated with each disease prediction. The specific cancer relationship to miR-
813 2392 is highlighted in **Fig. S7**, relating miR-2392 expression with patient survival in a pan-
814 cancer analysis. **B)** Barplot of scores using our matrix completion model to predict small
815 molecules that affect miRNA expression. Higher scores indicate more predicted associations. **C)**
816 Barplot of the normalized connectivity map (CMAP) scores. We used transcripts induced by
817 miR-2392 overrepresented genes to query CMAP. Higher negative scores reflect a greater

818 reversal of the miR-2392 transcriptomic signature. Further details on model statistics and
819 performance are found in **Figs. S8 – S10**.

820

Supplemental Figures and Material

822

The UNC COVID-19 Pathobiology Consortium is comprised of:

824 Shannon M Wallet[1,2], Robert Maile[2,3], Matthew C Wolfgang[2,4], Robert S Hagan[4,5], Jason R
825 Mock[4,5], Natalie M Bowman[6], Jose L Torres-Castillo[5], Miriya K Love[5], Suzanne L Meinig[4], Will
826 Lovell[1], Colleen Rice[5], Olivia Mitchem[1], Dominique Burgess[1], Jessica Suggs[1], Jordan Jacobs[3]

827

828 [1]Department of Oral and Craniofacial Health Sciences, UNC Adams School of Dentistry,
829 University of North Carolina School of Medicine, Chapel Hill, NC, 27599, USA
830 [2]Department of Microbiology & Immunology, University of North Carolina School of Medicine,
831 Chapel Hill, NC, 27599, USA
832 [3]Department of Surgery, University of North Carolina School of Medicine, Chapel Hill, NC,
833 27599, USA
834 [4]Marsico Lung Institute, University of North Carolina at Chapel Hill, Chapel Hill, NC, 27599,
835 USA
836 [5]Division of Pulmonary Diseases and Critical Care Medicine, Department of Medicine,
837 University of North Carolina, Chapel Hill, NC 27599, USA
838 [6]Division of Infectious Disease, School of Medicine, University of North Carolina, Chapel Hill,
839 NC, 27599, USA

840

841 **Figure S1. Mitochondrial gene targets of miR-2392 and regulated pathways. Related to**
842 **Figure 3.** Differential gene expression analysis for all miR-2392 mitochondrial gene targets
843 significantly expressed in nasopharyngeal swab and autopsy COVID-19 patient tissues. The
844 heatmaps display the t-score statistics for comparing viral load vs negative patient sample for all
845 samples. Main gene clusters were determined through k-mean clustering. Nine main gene
846 clusters were determined and ShinyGO (Ge et al., 2020) was utilized to determine the pathways
847 for each cluster which are displayed on the top panel of the heatmap. Differentially expressed
848 genes are shown with at least one comparison demonstrating a significant adjusted p-value
849 (FDR<0.05) when comparing COVID-19 patients (high, medium or low viral loads) to non-
850 infected control patients (none). Mir-2392 gene targets only determined from miRmap.

851

852 **Figure S2. Inflammatory gene targets of miR-2392 and regulated pathways. Related to**
853 **Figure 3.** Differential gene expression analysis for all miR-2392 inflammatory gene targets
854 significantly expressed in nasopharyngeal swab and autopsy COVID-19 patient tissues. The
855 heatmaps display the t-score statistics for comparing viral load vs negative patient sample for all
856 samples. Main gene clusters were determined through k-mean clustering. Eight main gene
857 clusters were determined and ShinyGO (Ge et al., 2020) was utilized to determine the pathways
858 for each cluster which are displayed on the top panel of the heatmap. Differentially expressed
859 genes are shown with at least one comparison demonstrating a significant adjusted p-value

860   (FDR<0.05) when comparing COVID-19 patients (high, medium or low viral loads) to non-
861   infected control patients (none). Mir-2392 gene targets only determined from miRmap.

862

863   **Figure S3. Circulating miR-1-3p with COVID-19 patients compared to COVID-19 negative**
864   **patients. Related to Figure 5.** Droplet digital PCR (ddPCR) with specific primer for miR-1-3p
865   was performed on serum, urine, and nasopharyngeal swab samples (including other seasonal
866   coronavirus samples) from COVID-19 positive and negative patients. The miRNA concentration
867   are reported as copies/5ng RNA. **A)** The levels of miRNA-2392 in all tissues from patients
868   grouped as SARS-CoV-2 positive (SARS-nCoV-2) or negative (neg). Unadjusted t-tests
869   comparing the SARS-CoV-2 positive to neg for each tissue are provided and also adjusted
870   statistics comparing the groups with a mixed model corrected for age and sex is provided. **B)**
871   Receiver Operating Characteristic (ROC) curve is provided for miR-1-3p for each tissue
872   comparing SARS-CoV-2 positive to negative patients. **C)** Comparing specific categories within
873   each tissue type between COVID-19 positive and negative patients. N = COVID-19 Negative, P
874   = COVID-19 positive, P_{int} = intubated patients, outp = outpatient, ICU = Intensive care
875   unit/inpatient, Cold = Coronaviruses related to the common cold, NL63 = NL63 coronavirus, and
876   CoV-2 = SARS-CoV-2. For all plots * = $p < 0.05$, ** = $p < 0.01$, and *** = $p < 0.001$.

877

878   **Figure S4. Circulating miR-155-5p with COVID-19 patients compared to COVID-19**
879   **negative patients. Related to Figure 5.** Droplet digital PCR (ddPCR) with specific primer for
880   miR-155-5p was performed on serum, urine, and nasopharyngeal swab samples (including other
881   seasonal coronavirus samples) from COVID-19 positive and negative patients. The miRNA
882   concentration are reported as copies/5ng RNA. **A)** The levels of miRNA-2392 in all tissues from
883   patients grouped as SARS-CoV-2 positive (SARS-nCoV-2) or negative (neg). Unadjusted t-tests
884   comparing the SARS-CoV-2 positive to neg for each tissue are provided and also adjusted
885   statistics comparing the groups with a mixed model corrected for age and sex is provided. **B)**
886   Receiver Operating Characteristic (ROC) curve is provided for miR-155-5p for each tissue
887   comparing SARS-CoV-2 positive to negative patients. **C)** Comparing specific categories within
888   each tissue type between COVID-19 positive and negative patients. N = COVID-19 Negative, P
889   = COVID-19 positive, P_{int} = intubated patients, outp = outpatient, ICU = Intensive care
890   unit/inpatient, Cold = Coronaviruses related to the common cold, NL63 = NL63 coronavirus, and
891   CoV-2 = SARS-CoV-2. For all plots * = $p < 0.05$, ** = $p < 0.01$, and *** = $p < 0.001$.

892

893   **Figure S5. Circulating miR-124-3p with COVID-19 patients compared to COVID-19**
894   **negative patients. Related to Figure 5.** Droplet digital PCR (ddPCR) with specific primer for
895   miR-124-3p was performed on serum, urine, and nasopharyngeal swab samples (including other
896   seasonal coronavirus samples) from COVID-19 positive and negative patients. The miRNA
897   concentration are reported as copies/5ng RNA. For miR-124-3p, the copies/5ng were either equal
898   to 0 or at extremely low levels close to 0 copies/5ng. To try to determine any statistical
899   differences we categorized the groups as ND = Not Determined which are all 0 values or D =
900   Determined which are values > 0 for both N = negative (open symbols) and P = COVID-19
901   positive patients samples (closed symbols). The number of patients for each column is shown

above the points. No significant differences were observed for any of the sample for miR-124-3p.

Figure S6. miR-2392 expression pan-cancer survival analysis. Related to Figure 7. Kaplan Meier patient survival plots for miR-2392 expression in a pan-cancer analysis was determined utilizing The Kaplan Meier plotter (Nagy et al., 2021). The plots were separated with the top row being cancers which patients had significantly poor survival with high expression of miR-2392, the middle row being cancers which patients had poor survival (but not significant) with high expression of miR-2392, and the bottom row being cancers which patients had significantly better survival with high expression of miR-2392.

Figure S7. Small molecules-miRNA dataset statistics Related to Figure 7. (Left) Number of small molecules associated to miRNAs. (Right) Number of miRNAs associated to small molecules.

Figure S8. Performance of our method at predicting missing small molecule-miRNA interactions. Related to Figure 7. (Top) The mean value of the Receiver Operating Curve (ROC) is shown for a ten-fold cross-validation experiment (dark blue). 95% confidence interval is also shown (light blue). (Bottom) The mean value of the Precision-Recall Curve (PRC) is shown for a ten-fold cross-validation experiment (dark salmon). 95% confidence interval is also shown (light salmon).

Figure S9. Performance of our method at predicting missing small molecule-miRNA interactions when controlling for data imbalance. Related to Figure 7. (Top) Area Under the Receiver Operating Curve (AUROC) was obtained in a ten-fold cross-validation experiment for varying values of the negative to positive label ratio in the test set. (Bottom) Area Under the Precision-Recall Curve (AUROC) was obtained in a ten-fold cross-validation experiment for varying values of the negative to positive label ratio in the test set.

Table S1. Annealing temperatures for miRNA primers, related to methods and Figure 5. Temperatures used for droplet digital PCR to quantify each miRNA target.

STAR⬛Methods

RESOURCE AVAILABILITY
Lead Contact
    Further information and requests for resources and reagents should be directed to and will be fulfilled by the Lead Contact, Afshin Beheshti (afshin.beheshti@nasa.gov).

Materials Availability
    This study did not generate new unique reagents.

Data and Code Availability

22

The published article includes all datasets generated and analyzed during this study. Processed bulk RNA-seq data is available online (https://covidgenes.weill.cornell.edu/). RNA-Seq alignment script for BALF samples and SHSY-5Y cells studies are attached. Limma script for SHSY5Y studies is attached.

EXPERIMENTAL MODEL AND SUBJECT DETAILS

Human serum and nasopharyngeal swab sample collection for ddPCR

All plasma and nasal swab samples from those with COVID-19 infection, seasonal coronavirus infection, and controls were collected from inpatients at the University of Maryland Medical Center, in Baltimore, USA, between March and May of 2020. Sample collection obtained through informed consent waiver, which was approved by the University of Maryland, Baltimore IRB.

For serum samples, N=10 samples from COVID-19 intubated patients, COVID-19 outpatients, and COVID-19 negative patients were obtained. An equal distribution of N=5 males and females were used for each group. Also, an equal age distribution of patients from 27 to 85 years old was utilized for each group.

For the nasopharyngeal samples the following patient samples were obtained: N=10 SARS-CoV-2 positive patients, N=6 common cold coronavirus samples, and N=6 Coronavirus NL63 samples. For the common cold coronavirus samples the breakdown was the following for the specific viruses: N=2 Coronavirus 229E, Coronavirus HKU1, and N=2 Coronavirus OC43.

Human nasopharyngeal swab sample collection for RNA-seq analysis

Patient specimens were processed as described in Butler et al., 2020 (Butler et al., 2021). Briefly, nasopharyngeal swabs were collected using the BD Universal Viral Transport Media system (Becton, Dickinson and Company, Franklin Lakes, NJ) from symptomatic patients. Total Nucleic Acid (TNA) was extracted from using automated nucleic acid extraction on the QIAsymphony and the DSP Virus/Pathogen Mini Kit (Qiagen).

Human autopsy tissue collection for RNA-seq analysis

The full methods of the patient sample collection from the autopsy patients are currently available in the Park et al. (Park et al., 2021). All autopsies are performed with consent of next of kin and permission for retention and research use of tissue. Autopsies were performed in a negative pressure room with protective equipment including N-95 masks; brain and bone were not obtained for safety reasons. All fresh tissues were procured prior to fixation and directly into Trizol for downstream RNA extraction. Tissues were collected from lung, liver, lymph nodes, kidney, and the heart as consent permitted. For GeoMx, RNAscope, trichrome and histology tissue sections were fixed in 10% neutral buffered formalin for 48 hours before processing and sectioning. These cases had a post-mortem interval of less than 48 hours. For bulk RNA-seq tissues, post-mortem intervals ranged from less than 24 hours to 72 hours (with 2 exceptions - one at 4 and one at 7 days - but passing RNA quality metrics) with an average of 2.5 days. All deceased patient remains were refrigerated at 4ºC prior to autopsy performance.

Human urine sample collection

Urine was collected from patients and volunteers at the University of North Carolina at Chapel Hill. All patients provided informed consent prior to participation in IRB-approved research protocols (UNC IRB: 20-0822 [RHS] and 20-0792 [NMB]). Mid-stream urine of outpatients and non-critically ill patients was collected by the clean catch method. Urine of intubated critically ill patients was collected from a port on the Foley catheter. Urine was aliquoted into 5 ml aliquots and stored at -80°C.

Urine aliquots were thawed, and microRNA was extracted from 1 ml per sample using Norgen Urine microRNA Purification Kit (Cat. 29000). Microalbumin and creatinine levels were assessed using Microalbumin 2-1 Combo strips (CLIAwaived Inc, cat# URS-2M).

Cell lines used for miR-2392 mimic experiments

Human SH-SY5Y cells were obtained from the ATCC and grown in Minimum Essential Medium (Gibco) / 10% FBS (Invitrogen) /1% MEM Non Essential Amino Acids (Gibco) / 1%GlutaMAX -l (Gibco). Cells were plated in 3.5 cm dishes and incubated with miR-2392 or control lentivirus particles (MOI 1) for 48h. Cells were harvested and lysed in Trizol reagent and RNA was extracted following manufacturers protocol (Invitrogen).

COVID-19 hamster model

Male Syrian hamsters 6-8 weeks old were utilized for efficacy studies with anti-miR-2392 FASTmer treatment. Three hamsters were used for each experimental group for a total of 30 hamsters with 10 treatment groups. Hamsters were infected with 10^5 pfu of SARS-CoV-2. There were 5 major treatment groups (N=6 per group) with two endpoints at day 3 or 7 post-viral challenge (N=3 per endpoint). Groups 1 and 3 were given the FASTmer treatment by IP injection while groups 2 and 4 were given by IN instillation under ketamine-xylazine anesthesia. Groups 1 and 2 were given single FASTmer treatment 24 hours before viral challenge. Groups 3 and 4 were given two doses of FASTmers at 24 hours before and 24 hours after viral challenge. The control group 5 was treated with PBS 24 hours prior to and 24 hours following viral challenge by IN instillation.

Treatment efficacy was assessed in multiple ways: 1) Change in daily body weight, 2) oropharyngeal shedding of virus on days 1-3 from all groups post-challenge assayed by plaque assay on Vero E6 cells (PFU/swab), 3) tissue burden of the virus at necropsy on day 3 from 2 lung tubes and turbinates assayed by plaque assay (PFU/100mg), and 4) histopathologic scoring on lungs and turbinates from all hamsters; the histopathological score for individual tissues, inflammation score from the interstitial lung inflammation, and total histopathological scores/assessment was made.

The dose of anti-miR-2392 that was used was calculated to raise blood levels to 10 μM if it were given intravenously. The molecular weight of anti-miR-2392 is 15,804. Assuming that hamsters weigh 120 grams and have 8% of body weight as blood, blood volume was approximately 0.01 liters. The dose per hamster was 1.58 mg in a 100 μl volume from an anti-miR-2392 solution.

1031 *In vitro viral screening model*
1032   A549-ACE2 cells, gifted by Dr. Brad Rosenberg (MSSM), were maintained in DMEM
1033 (Quality Biological, Gaithersburg, MD; #112-014-101) + 10% Fetal Bovine Serum (Gibco;
1034 #26140079) + 1% Penicillin-Streptomycin (Gemini Bio; #400-109). The day prior to treatment,
1035 5,000 A549-ACE2 cells were plated per well in 96-well plates. MiR-2932 was diluted in
1036 duplicate in A549-ACE2 media to a starting concentration of 20μM (Run 1) or 22μM (Runs 2
1037 and 3), and then an 8-point 1:2 dilution series was prepared. Media was removed from cells and
1038 90μL of each dilution was transferred to the cells. The plates were incubated for 2 hours at 37°C
1039 before being infected with an M.O.I. of 0.1 SARS-CoV-2 WA-1 (provided by Dr. Natalie
1040 Thornburg at the Centers for Disease Control and Prevention). Parallel plates were also run and
1041 left uninfected to monitor toxicity. Since Runs 2 and 3 were run simultaneously, a single toxicity
1042 plate was run for both. All plates were incubated at 37°C for 72 hours before being analyzed via
1043 Cell Titer Glo (Promega, Madison, WI; #G7573). Cell viability was compared to uninfected,
1044 untreated cells and infected, untreated cells.
1045
1046 **METHOD DETAILS**
1047
1048 *miRNA extraction for Droplet Digital PCR (ddPCR)*
1049   MiRNA extractions from serum were carried out using the Qiagen miRNeasy serum/plasma
1050 kit (#217184). MiRNA extractions from urine samples were carried out using Norgen urine
1051 microRNA Purification Kit (Cat. 29000, Norgen Bioteck Corp. Thorold, ON, Canada).
1052 Quantitation of miRNA samples was done using a NanoDrop 2000 Spectrophotometer
1053 (ThermoFisher Scientific).
1054
1055 *cDNA generation and ddPCR*
1056   First, cDNA was synthesized from miRNA samples using the Qiagen miRCURY LNA RT
1057 Kit (Cat. 339340) using a concentration of 5ng/μl for the miRNA per sample. Next, samples
1058 were mixed with a 1:20 dilution of the generated cDNA with the BioRad QX200 ddPCR
1059 Evagreen Supermix (Cat. 1864034) and the appropriate miRNA primers from miRCURY LNA
1060 miRNA PCR Assays (Qiagen). BioRad QX200 Automated Droplet Generator (Cat. 1864101)
1061 was used to create emulsion droplets. With the C1000 Touch™ Thermal Cycler with 96–Deep
1062 Well Reaction Module (Bio-Rad) the following PCR reaction was used for all the primers: 1
1063 cycle 95°C for 5 min, 40 cycles of 95°C for 30 sec and 58°C for 1 min (the annealing
1064 temperature can change depending on the primer), 1 cycle of 4°C for 5 min, and 1 cycle of 90°C
1065 for 5 min. Not all miRNA primers sets for ddPCR will have the same annealing temperature, so
1066 optimizing the annealing temperature is required for each primer set. Their respective annealing
1067 temperatures are found in **Table S1**. Finally, the QX200™ Droplet Digital™ PCR System (Bio-
1068 Rad) quantified the amount of miRNA for each primer set per sample. QuantaSoft software (Bio-
1069 Rad) generated the data for each primer set and sample. The same threshold setting was used for
1070 all samples per primer set. The concentration (miRNA copies/μl) value generated by QuantaSoft
1071 was converted to miRNA copies/ng of serum. These values were used for all miRNA analysis.
1072 For all analysis the miRNA concentrations were $\log_2(x+1)$ transformed to allow for easy
1073 comparison between miRNAs and samples.

1074

Publicly available Bronchial Alveolar Lavage Fluid (BALF) COVID-19 RNA-sequencing data

1075

1076 Fastq files were downloaded from SRA (NCBI BioProject PRJNA605907 (Shen et al., 2020)
1077 and NCBI BioProject PRJNA390194 (Ren et al., 2018)). Fastq data files were trimmed using
1078 TrimGalore v (0.6.4) with a quality cutoff of 30. Data were then aligned using STAR (v2.7.3)
1079 two pass mode to the Human reference genome (GRCh38 v99 downloaded 04-27-2020).
1080 Unaligned data were written to a fastq file, and then realigned to the GRCh38 reference genome
1081 using Bowtie 2 (v2.3.4.1), and output sam file converted to a bam file using samtools (v1.7). The
1082 resultant Bam files were merged, sorted, and read groups added using picard tools (v2.21.3)
1083 (script in supplemental data).

1084

Publicly available RNA-seq data: A549, Calu-3, NHBE, and COVID-19 lung biopsy

1085

1086 Raw RNA-seq read counts from the publication by Blanco-Melo *et al.* for the A549, Calu-3,
1087 and NHBE cell lines as well as post-mortem lung biopsies from two COVID-19 patients were
1088 downloaded from the Gene Expression Omnibus (series accession GSE147507) (Blanco-Melo et
1089 al., 2020).

1090

RNA-seq of Nasopharyngeal Swab COVID-19 patient samples

1091

1092 RNA isolation and library preparation is fully described in Butler, et al. (Butler et al., 2021).
1093 Briefly, library preparation on the all nasopharyngeal swab samples' total nucleic acid (TNA)
1094 were treated with DNAse 1 (Zymo Research, Catalog # E1010). Post-DNAse digested samples
1095 were then put into the NEBNext rRNA depletion v2 (Human/Mouse/Rat), Ultra II Directional
1096 RNA (10☐ng), and Unique Dual Index Primer Pairs were used following the vendor protocols
1097 from New England Biolabs. Kits were supplied from a single manufacturer lot. Completed
1098 libraries were quantified by Qubit or equivalent and run on a Bioanalyzer or equivalent for size
1099 determination. Libraries were pooled and sent to the WCM Genomics Core or HudsonAlpha for
1100 final quantification by Qubit fluorometer (ThermoFisher Scientific), TapeStation 2200 (Agilent),
1101 and qRT-PCR using the Kapa Biosystems Illumina library quantification kit.

1102

RNA-seq of COVID-19 autopsy tissue samples

1103

1104 RNA isolation and library preparation is fully described in Park, et al. (Park et al., 2021).
1105 Briefly, autopsy tissues were collected from lung, liver, lymph nodes, kidney, and the heart and
1106 were placed directly into Trizol, homogenized and then snap frozen in liquid nitrogen. At least
1107 after 24 hours these tissue samples were then processed via standard protocols to isolate RNA.
1108 New York Genome Center RNA sequencing libraries were prepared using the KAPA Hyper
1109 Library Preparation Kit + RiboErase, HMR (Roche) in accordance with manufacturer's
1110 recommendations. Briefly, 50-200ng of Total RNA were used for ribosomal depletion and
1111 fragmentation. Depleted RNA underwent first and second strand cDNA synthesis followed by
1112 adenylation, and ligation of unique dual indexed adapters. Libraries were amplified using 12
1113 cycles of PCR and cleaned-up by magnetic bead purification. Final libraries were quantified
1114 using fluorescent-based assays including PicoGreen (Life Technologies) or Qubit Fluorometer
1115 (Invitrogen) and Fragment Analyzer (Advanced Analytics) and sequenced on a NovaSeq 6000
1116 sequencer (v1 chemistry) with 2x150bp targeting 60M reads per sample.

miR-2392 mimic experiments in SH-SY5Y cells and RNA-seq

RNA was dissolved in nuclease free water and concentration determined spectrometrically at 260nm using a Biotek plate reader (Biotek). 500ng RNA was used as input for a whole transcriptome library preparation (ThermoFisher Total RNA). Libraries were quantified using a bioanalyzer chip reader (nanoDNA chips: Aglient Technologies) and diluted to 100 pM final concentration. Barcoded libraries were combined and use to seed a OneTouch bead templating reaction (OneTouch2). Cloned libraries were enriched and loaded on 540 Ion Torrent chips. Data were sequenced using the Ion Torrent RNA-seq workflow. Unaligned Bam files were converted to fatsq and aligned to the Grch 38 reference genome using STAR Two pass approach (Dobin paper) to create gene count tables as described in Overbery et al. (Overbey et al., 2021) (script in supplementary).

Anti-miR-2392 FASTmer inhibitor design and construction

The FAST (Facile Accelerated Specific Therapeutics) platform was used to design FASTmer inhibitors, which are composed of a nanobiohydrd molecule based on antisense peptide nucleic acid (PNA) moiety conjugated to nanoparticle for improved delivery and membrane transport. The PNA moiety was chosen to be 15 bases long (in order to maximize both solubility and specificity), which yielded six potential target sequences within the 20-nucleotide mature human miR-2392. These potential targets were screened using FAST for solubility, self-complementing sequences, and off-targeting within the human genome (GCF_000001405.26) and SARS-CoV-2 viral genome (NC_045512). The antisense sequence complementing miR-2392 nucleotides 2 to 16 (TCTCACCCCCATCCT) was chosen in order to minimize off-targeting while maximizing coverage of the miR-2392 seed region. The FASTmer was synthesized (with an N-terminal histidine tag and a 2-(2-(2-aminoethoxy)ethoxy)acetic acid linker) on an Apex 396 peptide synthesizer (AAPPTec, LLC) with solid-phase Fmoc chemistry. Fmoc-PNA monomers were obtained from PolyOrg Inc., with A, C, and G monomers protected with Bhoc groups. Following synthesis, the peptides were conjugated with nanoparticles and purified via size-exclusion filtration. Conjugation and concentration of the purified solution was monitored through measurement of absorbance at 260 nm (for detection of PNA) and 400 nm (for quantification of gold nanoparticles).

QUANTIFICATION AND STATISTICAL ANALYSIS

Analysis of BALF RNA-seq data

Bam files were imported into Partek Genome Studio v7.0, and gene expression values quantified vs the Grch38 reference annotation guide (Ensembl v99). Samples with fewer than 2 million aligned reads were excluded from further analysis. Genes with fewer than 10 reads in 25% of samples were excluded, and differential gene expression determined using ANOVA with infection status as contrast. Differentially expressed gene files were used in GSEA and IPA to determine biological significance and pathways being regulated.

Analysis of Nasopharyngeal Swab RNA-seq data

27

1160   The nasopharyngeal swab samples were analyzed comparing COVID-19 viral infection to
1161   the negative patients and was as previously described in Butler et al. (Butler et al., 2021) and the
1162   DESeq2 (Love et al., 2014) was utilized to generate the differential expression data. Heatmaps
1163   were displayed using pheatmap (Kolde, 2015). Volcano plots were made use R program
1164   EnhancedVolcano (Blighe et al., 2018).
1165

1166   *Analysis of Autopsy RNA-seq data*
1167   The full methods of the analysis from the autopsy patients is currently available in the Park et
1168   al. (Park et al., 2021). Briefly, RNA-seq data was processed through the nf-core/rnaseq pipeline
1169   (Ewels et al., 2020). This workflow involved adapter trimming using Trim Galore!
1170   (https://github.com/FelixKrueger/TrimGalore), read alignment with STAR (Dobin et al., 2013),
1171   gene quantification with Salmon (Patro et al., 2017), duplicate read marking with Picard
1172   MarkDuplicates (https://github.com/broadinstitute/picard), and transcript quantification with
1173   StringTie (Kovaka et al., 2019). Other quality control measures included RSeQC, Qualimap, and
1174   dupRadar. Alignment was performed using the GRCh38 build native to nf-core and annotation
1175   was performed using Gencode Human Release 33 (GRCH38.p13). FeatureCounts reads were
1176   normalized using variance-stabilizing transform (vst) in DESeq2 package in R for visualization
1177   purposes in log-scale (Love et al., 2014). Differential expression of genes were calculated by
1178   DESeq2. Differential expression comparisons were done as either COVID+ cases versus
1179   COVID- controls for each tissue specifically, correcting for sequencing batches with a covariate
1180   where applicable, or pairwise comparison of viral levels from the lung as determined by
1181   nCounter data. Volcano plots were made use R program EnhancedVolcano (Blighe et al., 2018).
1182

1183   *Analysis Combining Autopsy and Nasopharyngeal Swab RNA-seq data*
1184   To combine the results from the autopsy and nasopharyngeal swab RNA-seq data, we utilized
1185   the t-score values from the DESeq2 analysis. Heatmaps were displayed using pheatmap (Kolde,
1186   2015).
1187

1188   *Gene Set Enrichment Analysis (GSEA)*
1189   For pathway analysis on the miR-2392 targets (**Fig. 3**) we utilized ShinyGO (Ge et al., 2020)
1190   to determine the significantly regulated pathways for each main cluster in the heatmap. The
1191   clustering was determined through k-mean statistics.
1192   For pathway analysis on the miR-2392 mimic RNA-seq data, we utilized fast Gene Set
1193   Enrichment Analysis (fGSEA) (Korotkevich et al., 2021). Pathway analysis was done comparing
1194   miR-2392 mimics to all controls and the ranked list of genes were defined by the t-score
1195   statistics. The statistical significance was determined by 1000 permutations of the genesets
1196   (Subramanian et al., 2005).
1197

1198   *Analysis of proteomic and transcriptomic blood datasets from COVID-19 patients*
1199   For the analysis of the miR-2392 targets in the blood tissue, we downloaded whole blood
1200   transcriptome data and plasma proteome data from The COVIDome Explorer Researcher Portal
1201   (Sullivan et al., 2021). For Transcriptome data we used the following filters: Category "Effect of
1202   COVID-19 status", Platform "Blood", Statistical test "Student's t-test", Adjustment method

1203 "none", Sex "male" and "female", Age Group "All". For Proteome data we used the following
1204 filters: Category "Effect of COVID-19 status", Platform "SOMAscan", Statistical test "Student's
1205 t-test", Adjustment method "none", Sex "male" and "female", Age Group "All". We created the
1206 list of the intersecting genes from both datasets. We analyzed the list using RStudio Desktop
1207 1.3.1093 (RStudio Team (2020). RStudio: Integrated Development Environment for R. RStudio,
1208 PBC, Boston, MA URL http://www.rstudio.com/), and visualized data using ggplot2 version
1209 3.3.2 (Wickham, 2016) and ggrepel version 0.8.2 (https://ggrepel.slowkow.com/).
1210
1211 *Analysis of Monocyte RNA-seq data*
1212   The monocyte COVID-19 RNA-Seq data, published under the accession GSE159678
1213 (Rother et al., 2020), was downloaded from SRA and gene expression was quantified using
1214 Salmon's selective alignment approach (Srivastava et al., 2020). The RNA-Seq processing
1215 pipeline was implemented using pyrpipe (Singh et al., 2021) (https://github.com/urmi-
1216 21/pyrpipe/tree/master/case_studies/Covid_RNA-Seq). Exploratory data analysis and differential
1217 expression analysis were performed using MetaOmGraph (Singh et al., 2020).
1218
1219 *Analysis of A549, Calu-3, NHBE, and COVID lung biopsy data*
1220   Each data series was normalized and filtered for low-expressed genes (counts<1). Cell
1221 culture samples treated with SARS-CoV-2 were compared to untreated controls and COVID-19-
1222 positive patient samples were compared to healthy lung biopsies. Differentially expressed genes
1223 were determined from the R-program Limma-Voom (Ritchie et al., 2015) using a linear model
1224 with weighted least squares for each gene and the false discovery rate adjusted p-values were
1225 calculated.
1226
1227 *Analysis of miR-2392 mimic RNA-seq data*
1228   Differential gene expression was determined using LIMMA-voom (Ritchie et al., 2015).
1229 Data were filtered to ensure data contained at least 5 million aligned reads, and average gene
1230 counts of > 10. Cell treatments we used as contrasts for differentially expressed gene
1231 calculations. These results were then uploaded to GSEA for further analysis. (R script in
1232 supplementary section)
1233
1234 *Conservation of miR-2392 between species*
1235   To determined conservation of miR-2392 among different species we utilized UCSC
1236 Genome Browser (Kent et al., 2002). Hsa-miR-2392 was entered as an input and a select of
1237 species was used to compare which included common species that are currently used in SARS-
1238 CoV-2 *in vivo* studies (i.e. mice, ferrets, and hamsters). We also chose primates and other
1239 animals to provide a wide spectrum of species to observe conservation of miR-2392. Lastly, the
1240 USCS Genome Browser provides the host gene for miR-2392 (i.e. MEG3) and redirects to GTEx
1241 (Consortium, 2020) to provide a plot of MEG3 levels based on RNA-seq data on normal tissues.
1242
1243 *Mapping miR-2392 sequence to SARS-CoV-2 sequences*
1244   To explore potential binding sites for miR-2392 we used miRanda software (Enright et al.,
1245 2003) to identify all potential binding sites with respect to the SARS-CoV-2 reference genome

1246 (Wuhan-Hu-1; NC045512.2) and representative genomes from lineages of concern. The lineages
1247 of concern were selected from Global Initiative on Sharing All Influenza Data (GISAID) with
1248 each lineage being represented by 14 recent genomes.
1249
1250 *In silico predictions of genes from miRNAs*
1251 Through the use of a Cytoscape (Shannon et al., 2003) plug-in called ClueGo/CluePedia
1252 (Bindea et al., 2013), we were able to predict genes targeted by the miRNAs determined. This
1253 involved entering all miRNAs in ClueGo and allowing the software to determine the top 50
1254 genes that were significantly regulated and connected to the miRNAs. The predictions only
1255 reflect the functions that will be regulated by the miRNAs and do not show whether the function
1256 will be activated or inhibited. Lastly, miRNet 2.0 was utilized to predict the diseases and
1257 pathways that are associated with the miRNAs (Chang et al., 2020a). This was plotted as a dot
1258 utilizing the R-program ggplot2 (v3.2.1) (Wickham, 2016).
1259
1260 *ddPCR analysis of miRNA levels in patient samples*
1261 First, we normalized the amount of each miRNA measured per body location (nasal, serum,
1262 and urine) using the general logarithm transformation. We compared miRNA levels in samples
1263 from patients either positive or negative for SARS-nCoV-2 using the student's t-test (unadjusted)
1264 as well as controlling for sex and age using least squares adjustment. Next, we generated receiver
1265 operating characteristic curves from each body location to show the performance of a
1266 classification model (SARS-nCoV-2 positive versus negative) at all classification thresholds
1267 using the absolute, non-transformed levels (miRNA copies per 5 ng RNA). Finally, we
1268 performed a subanalysis on each location to compare the variance of each miRNA in SARS-
1269 nCoV-2 negative patients compared to other patient groups. For serum and nasal samples, 1-way
1270 ANOVA was used to identify variation associated with the patient classification. For urine
1271 samples, 2-way ANOVA was used with location (outpatient versus inpatient) and SARS-nCoV-2
1272 positivity as the main factors. If the ANOVA yielded a $P < 0.05$, Dunnett's post-test was used to
1273 compare subgroup means to the negative patient sample mean.
1274
1275 *Computational drug repositioning model*
1276 Using the SM2miR database (Liu et al., 2013), we assembled an $n \times m$ binary matrix (X)
1277 containing 3,593 associations between small molecules ($n = 213$, rows) and miRNAs ($m = 1,519$, columns). Each matrix entry (X_{ij}) was assigned a value of 1 where a small molecule is
1278 1,519, columns). Each matrix entry (X_{ij}) was assigned a value of 1 where a small molecule is
1279 known to be associated to miRNA, and was 0 otherwise. The chemical notation as a simplified
1280 molecular input line entry system (SMILES) was obtained for each small molecule from
1281 PubChem. We then calculated the 2D Tanimoto chemical similarity between pairs of small
1282 molecules using the MACCS key binary fingerprints with RDKit (RDKit: Open-source
1283 cheminformatics; http://www.rdkit.org). Similarly, for each miRNA, we obtained its sequence
1284 from miRbase (Kozomara et al., 2019) and computed sequence similarity between miRNAs as
1285 the score of their Needleman-Wunsch alignment. We used the binary matrix, together with the
1286 chemical and sequence similarities, as input to our state-of-the-art drug target prediction model
1287 to predict missing associations in X (Galeano et al., 2021). The model parameters where: $p = \frac{1}{2}$,

1288 $\beta_{Chem} = 1$, and $\alpha_{seq} = 0$. To assess the prediction performance of the model, we performed ten-
1289 fold cross-validation simulations.

1290

1291 **References**

1292 Allegra, L., Dal Sasso, M., Bovio, C., Massoni, C., Fonti, E., and Braga, P.C. (2002). Human
1293 neutrophil oxidative bursts and their in vitro modulation by different N-acetylcysteine
1294 concentrations. Arzneimittelforschung *52*, 669-676.

1295 Ardestani, A., and Azizi, Z. (2021). Targeting glucose metabolism for treatment of COVID-19.
1296 Signal Transduct Target Ther *6*, 112.

1297 Asai, A., Konno, M., Ozaki, M., Otsuka, C., Vecchione, A., Arai, T., Kitagawa, T., Ofusa, K.,
1298 Yabumoto, M., Hirotsu, T.*, et al.* (2020). COVID-19 Drug Discovery Using Intensive
1299 Approaches. Int J Mol Sci *21*.

1300 Aunins, T.R., Erickson, K.E., and Chatterjee, A. (2020). Transcriptome-based design of
1301 antisense inhibitors potentiates carbapenem efficacy in CRE Escherichia coli. Proc Natl Acad Sci
1302 U S A *117*, 30699-30709.

1303 Aykin-Burns, N., Franklin, E.A., and Ercal, N. (2005). Effects of N-acetylcysteine on lead-
1304 exposed PC-12 cells. Arch Environ Contam Toxicol *49*, 119-123.

1305 Baden, L.R., El Sahly, H.M., Essink, B., Kotloff, K., Frey, S., Novak, R., Diemert, D., Spector,
1306 S.A., Rouphael, N., Creech, C.B.*, et al.* (2021). Efficacy and Safety of the mRNA-1273 SARS-
1307 CoV-2 Vaccine. N Engl J Med *384*, 403-416.

1308 Bartoszewski, R., Dabrowski, M., Jakiela, B., Matalon, S., Harrod, K.S., Sanak, M., and
1309 Collawn, J.F. (2020). SARS-CoV-2 may regulate cellular responses through depletion of specific
1310 host miRNAs. Am J Physiol Lung Cell Mol Physiol *319*, L444-L455.

1311 Bindea, G., Galon, J., and Mlecnik, B. (2013). CluePedia Cytoscape plugin: pathway insights
1312 using integrated experimental and in silico data. Bioinformatics *29*, 661-663.

1313 Bindea, G., Mlecnik, B., Hackl, H., Charoentong, P., Tosolini, M., Kirilovsky, A., Fridman,
1314 W.H., Pages, F., Trajanoski, Z., and Galon, J. (2009). ClueGO: a Cytoscape plug-in to decipher
1315 functionally grouped gene ontology and pathway annotation networks. Bioinformatics *25*, 1091-
1316 1093.

1317 Blanco-Melo, D., Nilsson-Payant, B.E., Liu, W.C., Uhl, S., Hoagland, D., Moller, R., Jordan,
1318 T.X., Oishi, K., Panis, M., Sachs, D.*, et al.* (2020). Imbalanced Host Response to SARS-CoV-2
1319 Drives Development of COVID-19. Cell *181*, 1036-1045 e1039.

1320 Blighe, K., Rana, S., and Lewis, M. (2018). EnhancedVolcano: Publication-ready volcano plots
1321 with enhanced colouring and labeling. https://github.com/kevinblighe/EnhancedVolcano.

1322 Butler, D., Mozsary, C., Meydan, C., Foox, J., Rosiene, J., Shaiber, A., Danko, D., Afshinnekoo,
1323 E., MacKay, M., Sedlazeck, F.J.*, et al.* (2021). Shotgun transcriptome, spatial omics, and
1324 isothermal profiling of SARS-CoV-2 infection reveals unique host responses, viral
1325 diversification, and drug interactions. Nat Commun *12*, 1660.

1326 Carboni, E., Carta, A.R., and Carboni, E. (2020). Can pioglitazone be potentially useful
1327 therapeutically in treating patients with COVID-19? Med Hypotheses *140*, 109776.

1328 Carfi, A., Bernabei, R., Landi, F., and Gemelli Against, C.-P.-A.C.S.G. (2020). Persistent
1329 Symptoms in Patients After Acute COVID-19. JAMA *324*, 603-605.

1330 Carrico, C., Meyer, J.G., He, W., Gibson, B.W., and Verdin, E. (2018). The Mitochondrial
1331 Acylome Emerges: Proteomics, Regulation by Sirtuins, and Metabolic and Disease Implications.
1332 Cell Metab *27*, 497-512.

1333 Centa, A., Fonseca, A.S., Ferreira, S., Azevedo, M.L.V., Vaz de Paula, C.B., Nagashima, S.,
1334 Machado-Souza, C., Miggiolaro, A., Baena, C.P., de Noronha, L.*, et al.* (2020). Deregulated
1335 miRNA expression is associated with endothelial dysfunction in post-mortem lung biopsies of
1336 COVID-19 patients. Am J Physiol Lung Cell Mol Physiol.

1337 Chang, L., Zhou, G., Soufan, O., and Xia, J. (2020a). miRNet 2.0: network-based visual
1338 analytics for miRNA functional analysis and systems biology. Nucleic Acids Res.

1339 Chang, L., Zhou, G., Soufan, O., and Xia, J. (2020b). miRNet 2.0: network-based visual
1340 analytics for miRNA functional analysis and systems biology. Nucleic Acids Res *48*, W244-
1341 W251.

1342 Chen, J., Yao, D., Li, Y., Chen, H., He, C., Ding, N., Lu, Y., Ou, T., Zhao, S., Li, L.*, et al.*
1343 (2013). Serum microRNA expression levels can predict lymph node metastasis in patients with
1344 early-stage cervical squamous cell carcinoma. Int J Mol Med *32*, 557-567.

1345 Chen, Y., and Wang, X. (2020). miRDB: an online database for prediction of functional
1346 microRNA targets. Nucleic Acids Res *48*, D127-D131.

1347 Condorelli, G., Latronico, M.V., and Dorn, G.W., 2nd (2010). microRNAs in heart disease:
1348 putative novel therapeutic targets? Eur Heart J *31*, 649-658.

1349 Consortium, G.T. (2020). The GTEx Consortium atlas of genetic regulatory effects across human
1350 tissues. Science *369*, 1318-1330.

1351 Dickey, L.L., Worne, C.L., Glover, J.L., Lane, T.E., and O'Connell, R.M. (2016). MicroRNA-
1352 155 enhances T cell trafficking and antiviral effector function in a model of coronavirus-induced
1353 neurologic disease. J Neuroinflammation *13*, 240.

1354 Dobin, A., Davis, C.A., Schlesinger, F., Drenkow, J., Zaleski, C., Jha, S., Batut, P., Chaisson,
1355 M., and Gingeras, T.R. (2013). STAR: ultrafast universal RNA-seq aligner. Bioinformatics *29*,
1356 15-21.

1357 Dweep, H., and Gretz, N. (2015). miRWalk2.0: a comprehensive atlas of microRNA-target
1358 interactions. Nat Methods *12*, 697.

1359 Edmonds, C.E., Zuckerman, S.P., and Conant, E.F. (2021). Management of Unilateral Axillary
1360 Lymphadenopathy Detected on Breast MRI in the Era of Coronavirus Disease (COVID-19)
1361 Vaccination. AJR Am J Roentgenol.

1362 Eller, K.A., Aunins, T.R., Courtney, C.M., Campos, J.K., Otoupal, P.B., Erickson, K.E.,
1363 Madinger, N.E., and Chatterjee, A. (2021). Facile accelerated specific therapeutic (FAST)
1364 platform develops antisense therapies to counter multidrug-resistant bacteria. Commun Biol *4*,
1365 331.

1366 Enomoto, Y., Takagi, R., Naito, Y., Kiniwa, T., Tanaka, Y., Hamada-Tsutsumi, S., Kawano, M.,
1367 Matsushita, S., Ochiya, T., and Miyajima, A. (2017). Identification of the novel 3' UTR
1368 sequences of human IL-21 mRNA as potential targets of miRNAs. Sci Rep *7*, 7780.

Enright, A.J., John, B., Gaul, U., Tuschl, T., Sander, C., and Marks, D.S. (2003). MicroRNA targets in Drosophila. Genome Biol *5*, R1.

Ewels, P.A., Peltzer, A., Fillinger, S., Patel, H., Alneberg, J., Wilm, A., Garcia, M.U., Di Tommaso, P., and Nahnsen, S. (2020). The nf-core framework for community-curated bioinformatics pipelines. Nat Biotechnol *38*, 276-278.

Fan, S., Tian, T., Chen, W., Lv, X., Lei, X., Zhang, H., Sun, S., Cai, L., Pan, G., He, L.*, et al.* (2019). Mitochondrial miRNA Determines Chemoresistance by Reprogramming Metabolism and Regulating Mitochondrial Transcription. Cancer research *79*, 1069-1084.

Feng, L., Yin, Y.Y., Liu, C.H., Xu, K.R., Li, Q.R., Wu, J.R., and Zeng, R. (2020). Proteome-wide Data Analysis Reveals Tissue-specific Network Associated with SARS-CoV-2 Infection. J Mol Cell Biol.

Friedman, R.C., Farh, K.K., Burge, C.B., and Bartel, D.P. (2009). Most mammalian mRNAs are conserved targets of microRNAs. Genome Res *19*, 92-105.

Galeano, D., Noto, S., Jimenez, R., and Paccanaro, A. (2021). Interpretable Drug Target Predictions using Self-Expressiveness. bioRxiv, 2021.2003.2001.433365.

Ge, S.X., Jung, D., and Yao, R. (2020). ShinyGO: a graphical gene-set enrichment tool for animals and plants. Bioinformatics *36*, 2628-2629.

Gharebaghi, R., Heidary, F., Moradi, M., and Parvizi, M. (2020). Metronidazole; a Potential Novel Addition to the COVID-19 Treatment Regimen. Arch Acad Emerg Med *8*, e40.

Griffin, R.J., Monzen, H., Williams, B.W., Park, H., Lee, S.H., and Song, C.W. (2003). Arsenic trioxide induces selective tumour vascular damage via oxidative stress and increases thermosensitivity of tumours. Int J Hyperthermia *19*, 575-589.

Gudbjartsson, D.F., Norddahl, G.L., Melsted, P., Gunnarsdottir, K., Holm, H., Eythorsson, E., Arnthorsson, A.O., Helgason, D., Bjarnadottir, K., Ingvarsson, R.F.*, et al.* (2020). Humoral Immune Response to SARS-CoV-2 in Iceland. N Engl J Med *383*, 1724-1734.

Gupta, A., Madhavan, M.V., Sehgal, K., Nair, N., Mahajan, S., Sehrawat, T.S., Bikdeli, B., Ahluwalia, N., Ausiello, J.C., Wan, E.Y.*, et al.* (2020). Extrapulmonary manifestations of COVID-19. Nat Med *26*, 1017-1032.

Hemmat, N., Asadzadeh, Z., Ahangar, N.K., Alemohammad, H., Najafzadeh, B., Derakhshani, A., Baghbanzadeh, A., Baghi, H.B., Javadrashid, D., Najafi, S.*, et al.* (2021). The roles of signaling pathways in SARS-CoV-2 infection; lessons learned from SARS-CoV and MERS-CoV. Archives of Virology *166*, 675-696.

Herrmann, J., Mori, V., Bates, J.H.T., and Suki, B. (2020). Modeling lung perfusion abnormalities to explain early COVID-19 hypoxemia. Nat Commun *11*, 4883.

Ho, W.Z., and Douglas, S.D. (1992). Glutathione and N-acetylcysteine suppression of human immunodeficiency virus replication in human monocyte/macrophages in vitro. AIDS Res Hum Retroviruses *8*, 1249-1253.

Hou, X., Liang, Y., Chen, J., Wei, Y., Zeng, P., Wang, L., Lu, C., and Diao, H. (2017). Expression Profiling of Cellular MicroRNA in Asymptomatic HBsAg Carriers and Chronic Hepatitis B Patients. Biomed Res Int *2017*, 6484835.

Hou, Z., Fan, F., and Liu, P. (2019). BTXA regulates the epithelial-mesenchymal transition and autophagy of keloid fibroblasts via modulating miR-1587/miR-2392 targeted ZEB2. Biosci Rep *39*.

Hu, H.M., Chen, Y., Liu, L., Zhang, C.G., Wang, W., Gong, K., Huang, Z., Guo, M.X., Li, W.X., and Li, W. (2013). C1orf61 acts as a tumor activator in human hepatocellular carcinoma and is associated with tumorigenesis and metastasis. FASEB J *27*, 163-173.

Hu, S., Li, Z., Lan, Y., Guan, J., Zhao, K., Chu, D., Fan, G., Guo, Y., Gao, F., and He, W. (2020). MiR-10a-5p-Mediated Syndecan 1 Suppression Restricts Porcine Hemagglutinating Encephalomyelitis Virus Replication. Front Microbiol *11*, 105.

Huang, C., Wang, Y., Li, X., Ren, L., Zhao, J., Hu, Y., Zhang, L., Fan, G., Xu, J., Gu, X.*, et al.* (2020). Clinical features of patients infected with 2019 novel coronavirus in Wuhan, China. Lancet *395*, 497-506.

Hultstrom, M., Lipcsey, M., Wallin, E., Larsson, I.M., Larsson, A., and Frithiof, R. (2021). Severe acute kidney injury associated with progression of chronic kidney disease after critical COVID-19. Crit Care *25*, 37.

Ibrahim, H., Perl, A., Smith, D., Lewis, T., Kon, Z., Goldenberg, R., Yarta, K., Staniloae, C., and Williams, M. (2020). Therapeutic blockade of inflammation in severe COVID-19 infection with intravenous N-acetylcysteine. Clin Immunol *219*, 108544.

Islam, M.S., and Islam, A.B.M.M.K. (2021). Viral miRNAs confer survival in host cells by targeting apoptosis related host genes. Informatics in Medicine Unlocked *22*, 100501.

Jacobs, L.G., Gourna Paleoudis, E., Lesky-Di Bari, D., Nyirenda, T., Friedman, T., Gupta, A., Rasouli, L., Zetkulic, M., Balani, B., Ogedegbe, C.*, et al.* (2020). Persistence of symptoms and quality of life at 35 days after hospitalization for COVID-19 infection. PLoS One *15*, e0243882.

Janssen, H.L., Reesink, H.W., Lawitz, E.J., Zeuzem, S., Rodriguez-Torres, M., Patel, K., van der Meer, A.J., Patick, A.K., Chen, A., Zhou, Y.*, et al.* (2013). Treatment of HCV infection by targeting microRNA. N Engl J Med *368*, 1685-1694.

Jia, D., Koonce, N.A., Griffin, R.J., Jackson, C., and Corry, P.M. (2010). Prevention and mitigation of acute death of mice after abdominal irradiation by the antioxidant N-acetyl-cysteine (NAC). Radiat Res *173*, 579-589.

Jiang, Q., Wang, Y., Hao, Y., Juan, L., Teng, M., Zhang, X., Li, M., Wang, G., and Liu, Y. (2009). miR2Disease: a manually curated database for microRNA deregulation in human disease. Nucleic Acids Res *37*, D98-104.

Jima, D.D., Zhang, J., Jacobs, C., Richards, K.L., Dunphy, C.H., Choi, W.W., Au, W.Y., Srivastava, G., Czader, M.B., Rizzieri, D.A.*, et al.* (2010). Deep sequencing of the small RNA transcriptome of normal and malignant human B cells identifies hundreds of novel microRNAs. Blood *116*, e118-127.

Johansen, M.D., Irving, A., Montagutelli, X., Tate, M.D., Rudloff, I., Nold, M.F., Hansbro, N.G., Kim, R.Y., Donovan, C., Liu, G.*, et al.* (2020). Animal and translational models of SARS-CoV-2 infection and COVID-19. Mucosal Immunol *13*, 877-891.

Jopling, C.L., Yi, M., Lancaster, A.M., Lemon, S.M., and Sarnow, P. (2005). Modulation of hepatitis C virus RNA abundance by a liver-specific MicroRNA. Science *309*, 1577-1581.

Kent, W.J., Sugnet, C.W., Furey, T.S., Roskin, K.M., Pringle, T.H., Zahler, A.M., and Haussler, D. (2002). The human genome browser at UCSC. Genome Res *12*, 996-1006.

Kharazmi, A., Nielsen, H., and Schiotz, P.O. (1988). N-acetylcysteine inhibits human neutrophil and monocyte chemotaxis and oxidative metabolism. Int J Immunopharmacol *10*, 39-46.

Kolde, R. (2015). pheatmap: Pretty heatmaps [Software].

Korotkevich, G., Sukhov, V., Budin, N., Shpak, B., Artyomov, M.N., and Sergushichev, A. (2021). Fast gene set enrichment analysis. bioRxiv, 060012.

Koumpa, F.S., Forde, C.T., and Manjaly, J.G. (2020). Sudden irreversible hearing loss post COVID-19. BMJ Case Rep *13*.

Kovaka, S., Zimin, A.V., Pertea, G.M., Razaghi, R., Salzberg, S.L., and Pertea, M. (2019). Transcriptome assembly from long-read RNA-seq alignments with StringTie2. Genome Biol *20*, 278.

Kozomara, A., Birgaoanu, M., and Griffiths-Jones, S. (2019). miRBase: from microRNA sequences to function. Nucleic Acids Res *47*, D155-D162.

Krajewski, P.K., Maj, J., and Szepietowski, J.C. (2021). Cutaneous Hyperaesthesia in SARS-CoV-2 Infection: Rare but not Unique Clinical Manifestation. Acta Derm Venereol *101*, adv00366.

Lamb, J., Crawford, E.D., Peck, D., Modell, J.W., Blat, I.C., Wrobel, M.J., Lerner, J., Brunet, J.P., Subramanian, A., Ross, K.N.*, et al.* (2006). The Connectivity Map: using gene-expression signatures to connect small molecules, genes, and disease. Science *313*, 1929-1935.

Lawrie, C.H., Gal, S., Dunlop, H.M., Pushkaran, B., Liggins, A.P., Pulford, K., Banham, A.H., Pezzella, F., Boultwood, J., Wainscoat, J.S.*, et al.* (2008). Detection of elevated levels of tumour-associated microRNAs in serum of patients with diffuse large B-cell lymphoma. Br J Haematol *141*, 672-675.

Ledford, H. (2020). Coronavirus breakthrough: dexamethasone is first drug shown to save lives. Nature *582*, 469.

Li, J., Li, T., Lu, Y., Shen, G., Guo, H., Wu, J., Lei, C., Du, F., Zhou, F., Zhao, X.*, et al.* (2017). MiR-2392 suppresses metastasis and epithelial-mesenchymal transition by targeting MAML3 and WHSC1 in gastric cancer. FASEB J *31*, 3774-3786.

Li, K., Chen, G., Hou, H., Liao, Q., Chen, J., Bai, H., Lee, S., Wang, C., Li, H., Cheng, L.*, et al.* (2021). Analysis of sex hormones and menstruation in COVID-19 women of child-bearing age. Reprod Biomed Online *42*, 260-267.

Liu, X., Wang, S., Meng, F., Wang, J., Zhang, Y., Dai, E., Yu, X., Li, X., and Jiang, W. (2013). SM2miR: a database of the experimentally validated small molecules' effects on microRNA expression. Bioinformatics *29*, 409-411.

Lott, M.T., Leipzig, J.N., Derbeneva, O., Xie, H.M., Chalkia, D., Sarmady, M., Procaccio, V., and Wallace, D.C. (2013). mtDNA Variation and Analysis Using Mitomap and Mitomaster. Curr Protoc Bioinformatics *44*, 1 23 21-26.

Love, M.I., Huber, W., and Anders, S. (2014). Moderated estimation of fold change and dispersion for RNA-seq data with DESeq2. Genome Biol *15*, 550.

1490 Loza, M.J., McCall, C.E., Li, L., Isaacs, W.B., Xu, J., and Chang, B.L. (2007). Assembly of
1491 inflammation-related genes for pathway-focused genetic analysis. PLoS One *2*, e1035.

1492 Ma, Y., Wang, C., Xue, M., Fu, F., Zhang, X., Li, L., Yin, L., Xu, W., Feng, L., and Liu, P.
1493 (2018). The Coronavirus Transmissible Gastroenteritis Virus Evades the Type I Interferon
1494 Response through IRE1alpha-Mediated Manipulation of the MicroRNA miR-30a-5p/SOCS1/3
1495 Axis. J Virol *92*.

1496 Mahajan, A., and Mason, G.F. (2021). A sobering addition to the literature on COVID-19 and
1497 the brain. J Clin Invest.

1498 Malik, Z.R., Razaq, Z., Siff, M., and Sheikh, S. (2020). COVID-19 Presenting as Banti's
1499 Syndrome. Cureus *12*, e9096.

1500 Mishra, P.K., Tandon, R., and Byrareddy, S.N. (2020). Diabetes and COVID-19 risk: an miRNA
1501 perspective. Am J Physiol Heart Circ Physiol *319*, H604-H609.

1502 Mitchell, P.S., Parkin, R.K., Kroh, E.M., Fritz, B.R., Wyman, S.K., Pogosova-Agadjanyan, E.L.,
1503 Peterson, A., Noteboom, J., O'Briant, K.C., Allen, A.*, et al.* (2008). Circulating microRNAs as
1504 stable blood-based markers for cancer detection. Proc Natl Acad Sci U S A *105*, 10513-10518.

1505 Nagy, A., Lanczky, A., Menyhart, O., and Gyorffy, B. (2018). Validation of miRNA prognostic
1506 power in hepatocellular carcinoma using expression data of independent datasets. Sci Rep *8*,
1507 9227.

1508 Nagy, A., Munkacsy, G., and Gyorffy, B. (2021). Pancancer survival analysis of cancer hallmark
1509 genes. Sci Rep *11*, 6047.

1510 Nersisyan, S., Engibaryan, N., Gorbonos, A., Kirdey, K., Makhonin, A., and Tonevitsky, A.
1511 (2020). Potential role of cellular miRNAs in coronavirus-host interplay. PeerJ *8*, e9994.

1512 Nishiga, M., Wang, D.W., Han, Y., Lewis, D.B., and Wu, J.C. (2020). COVID-19 and
1513 cardiovascular disease: from basic mechanisms to clinical perspectives. Nat Rev Cardiol *17*, 543-
1514 558.

1515 Ochsner, S.A., Pillich, R.T., and McKenna, N.J. (2020). Consensus transcriptional regulatory
1516 networks of coronavirus-infected human cells. Sci Data *7*, 314.

1517 Ottosen, S., Parsley, T.B., Yang, L., Zeh, K., van Doorn, L.J., van der Veer, E., Raney, A.K.,
1518 Hodges, M.R., and Patick, A.K. (2015). In vitro antiviral activity and preclinical and clinical
1519 resistance profile of miravirsen, a novel anti-hepatitis C virus therapeutic targeting the human
1520 factor miR-122. Antimicrob Agents Chemother *59*, 599-608.

1521 Park, J., Foox, J., Hether, T., Danko, D., Warren, S., Kim, Y., Reeves, J., Butler, D.J., Mozsary,
1522 C., Rosiene, J.*, et al.* (2021). Systemic Tissue and Cellular Disruption from SARS-CoV-2
1523 Infection revealed in COVID-19 Autopsies and Spatial Omics Tissue Maps. bioRxiv,
1524 2021.2003.2008.434433.

1525 Park, J.L., Park, S.M., Kwon, O.H., Lee, H.C., Kim, J.Y., Seok, H.H., Lee, W.S., Lee, S.H.,
1526 Kim, Y.S., Woo, K.M.*, et al.* (2014). Microarray screening and qRT-PCR evaluation of
1527 microRNA markers for forensic body fluid identification. Electrophoresis *35*, 3062-3068.

1528 Patro, R., Duggal, G., Love, M.I., Irizarry, R.A., and Kingsford, C. (2017). Salmon provides fast
1529 and bias-aware quantification of transcript expression. Nat Methods *14*, 417-419.
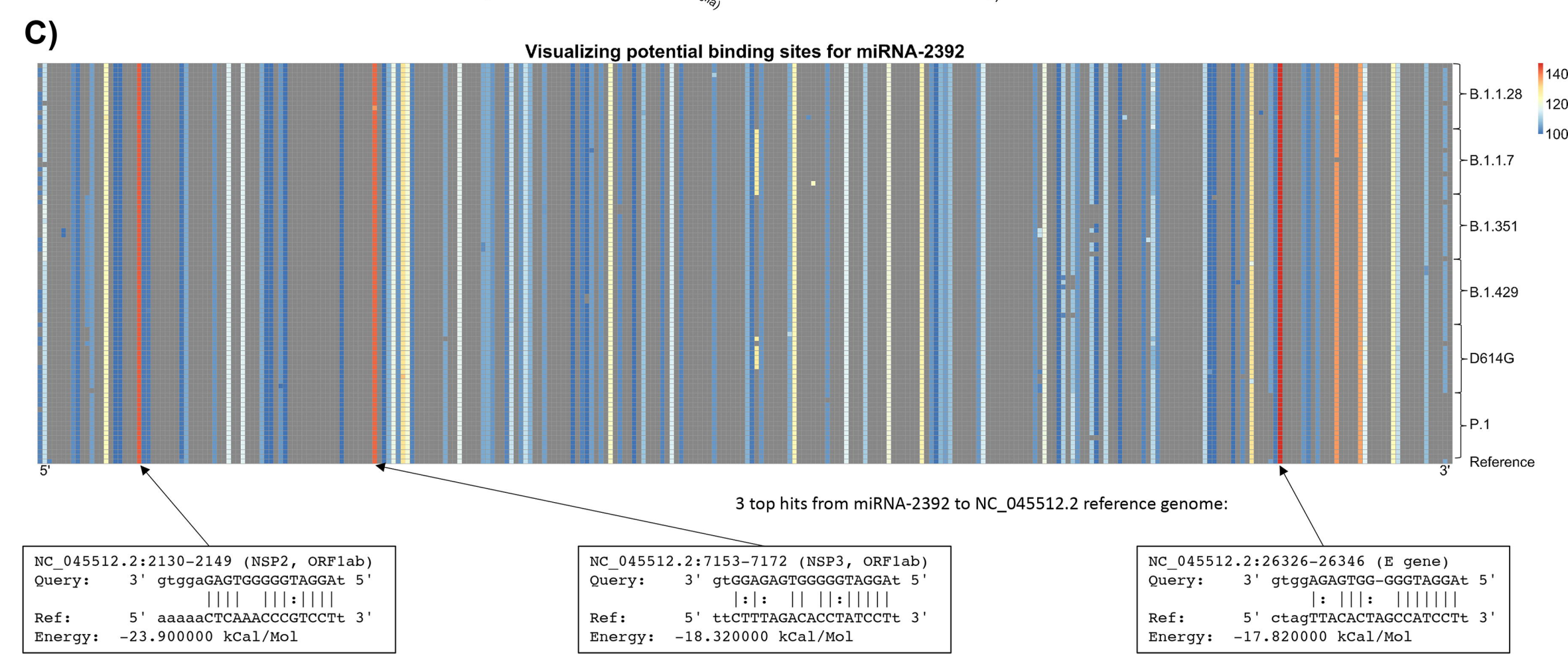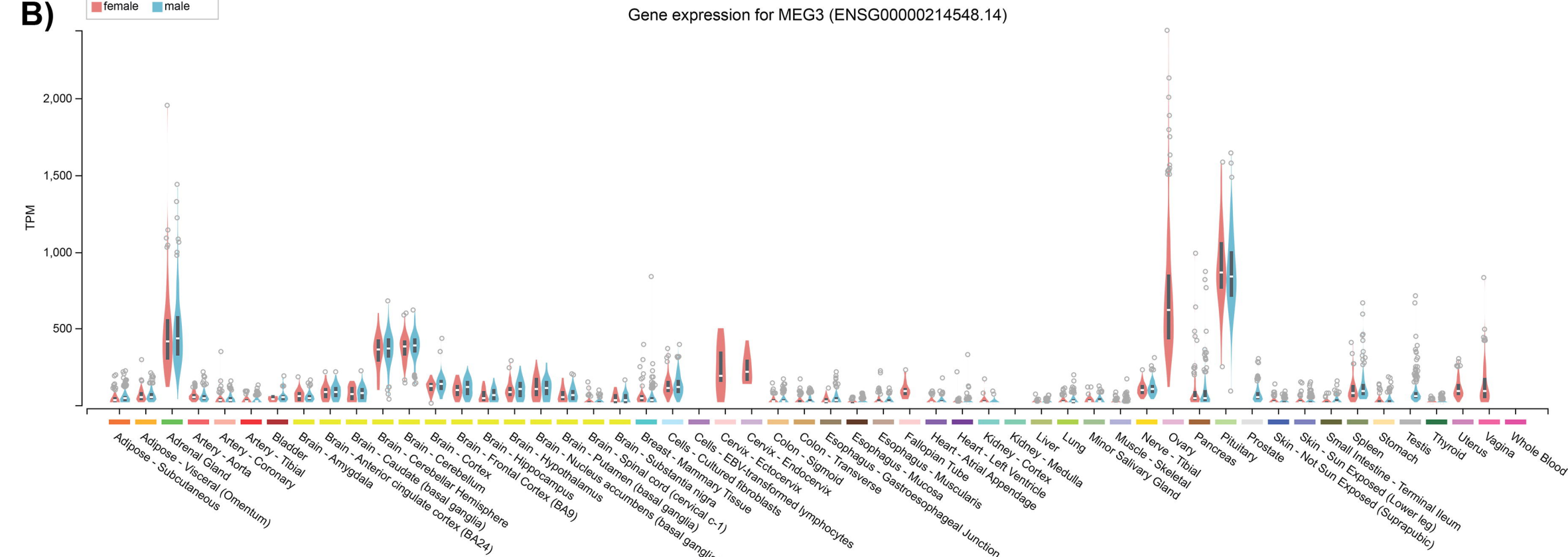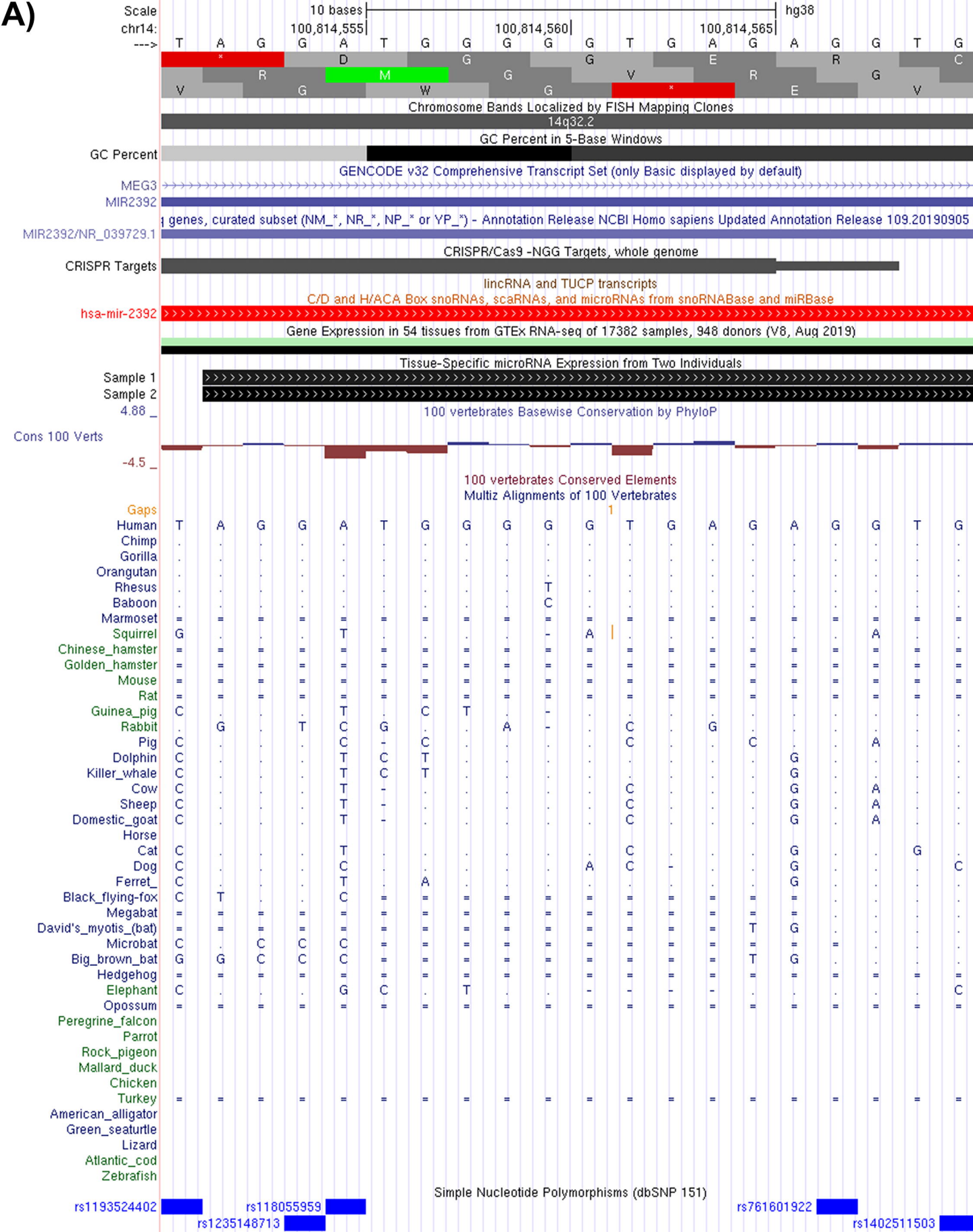
Polack, F.P., Thomas, S.J., Kitchin, N., Absalon, J., Gurtman, A., Lockhart, S., Perez, J.L., Perez Marc, G., Moreira, E.D., Zerbini, C.*, et al.* (2020). Safety and Efficacy of the BNT162b2 mRNA Covid-19 Vaccine. N Engl J Med *383*, 2603-2615.

Pontecorvi, G., Bellenghi, M., Ortona, E., and Care, A. (2020). microRNAs as new possible actors in gender disparities of Covid-19 pandemic. Acta Physiol (Oxf) *230*, e13538.

Poppe, M., Wittig, S., Jurida, L., Bartkuhn, M., Wilhelm, J., Muller, H., Beuerlein, K., Karl, N., Bhuju, S., Ziebuhr, J.*, et al.* (2017). The NF-kappaB-dependent and -independent transcriptome and chromatin landscapes of human coronavirus 229E-infected cells. PLoS Pathog *13*, e1006286.

Portincasa, P., Krawczyk, M., Machill, A., Lammert, F., and Di Ciaula, A. (2020). Hepatic consequences of COVID-19 infection. Lapping or biting? Eur J Intern Med *77*, 18-24.

Rath, S., Sharma, R., Gupta, R., Ast, T., Chan, C., Durham, T.J., Goodman, R.P., Grabarek, Z., Haas, M.E., Hung, W.H.W.*, et al.* (2021). MitoCarta3.0: an updated mitochondrial proteome now with sub-organelle localization and pathway annotations. Nucleic Acids Res *49*, D1541-D1547.

Rodriguez, M., Soler, Y., Perry, M., Reynolds, J.L., and El-Hage, N. (2020). Impact of Severe Acute Respiratory Syndrome Coronavirus 2 (SARS-CoV-2) in the Nervous System: Implications of COVID-19 in Neurodegeneration. Front Neurol *11*, 583459.

Rossi, R., Talarico, M., Coppi, F., and Boriani, G. (2020). Protective role of statins in COVID 19 patients: importance of pharmacokinetic characteristics rather than intensity of action. Intern Emerg Med *15*, 1573-1576.

Rother, N., Yanginlar, C., Lindeboom, R.G.H., Bekkering, S., van Leent, M.M.T., Buijsers, B., Jonkman, I., de Graaf, M., Baltissen, M., Lamers, L.A.*, et al.* (2020). Hydroxychloroquine Inhibits the Trained Innate Immune Response to Interferons. Cell Rep Med *1*, 100146.

Rupaimoole, R., and Slack, F.J. (2017). MicroRNA therapeutics: towards a new era for the management of cancer and other diseases. Nat Rev Drug Discov *16*, 203-222.

Sacar Demirci, M.D., and Adan, A. (2020). Computational analysis of microRNA-mediated interactions in SARS-CoV-2 infection. PeerJ *8*, e9369.

Sadoff, J., Le Gars, M., Shukarev, G., Heerwegh, D., Truyers, C., de Groot, A.M., Stoop, J., Tete, S., Van Damme, W., Leroux-Roels, I.*, et al.* (2021). Interim Results of a Phase 1-2a Trial of Ad26.COV2.S Covid-19 Vaccine. N Engl J Med.

Sadowska, A.M., Manuel-y-Keenoy, B., Vertongen, T., Schippers, G., Radomska-Lesniewska, D., Heytens, E., and De Backer, W.A. (2006). Effect of N-acetylcysteine on neutrophil activation markers in healthy volunteers: in vivo and in vitro study. Pharmacol Res *53*, 216-225.

Sardar, R., Satish, D., and Gupta, D. (2020). Identification of Novel SARS-CoV-2 Drug Targets by Host MicroRNAs and Transcription Factors Co-regulatory Interaction Network Analysis. Front Genet *11*, 571274.

Schult, P., Roth, H., Adams, R.L., Mas, C., Imbert, L., Orlik, C., Ruggieri, A., Pyle, A.M., and Lohmann, V. (2018). microRNA-122 amplifies hepatitis C virus translation by shaping the structure of the internal ribosomal entry site. Nat Commun *9*, 2613.
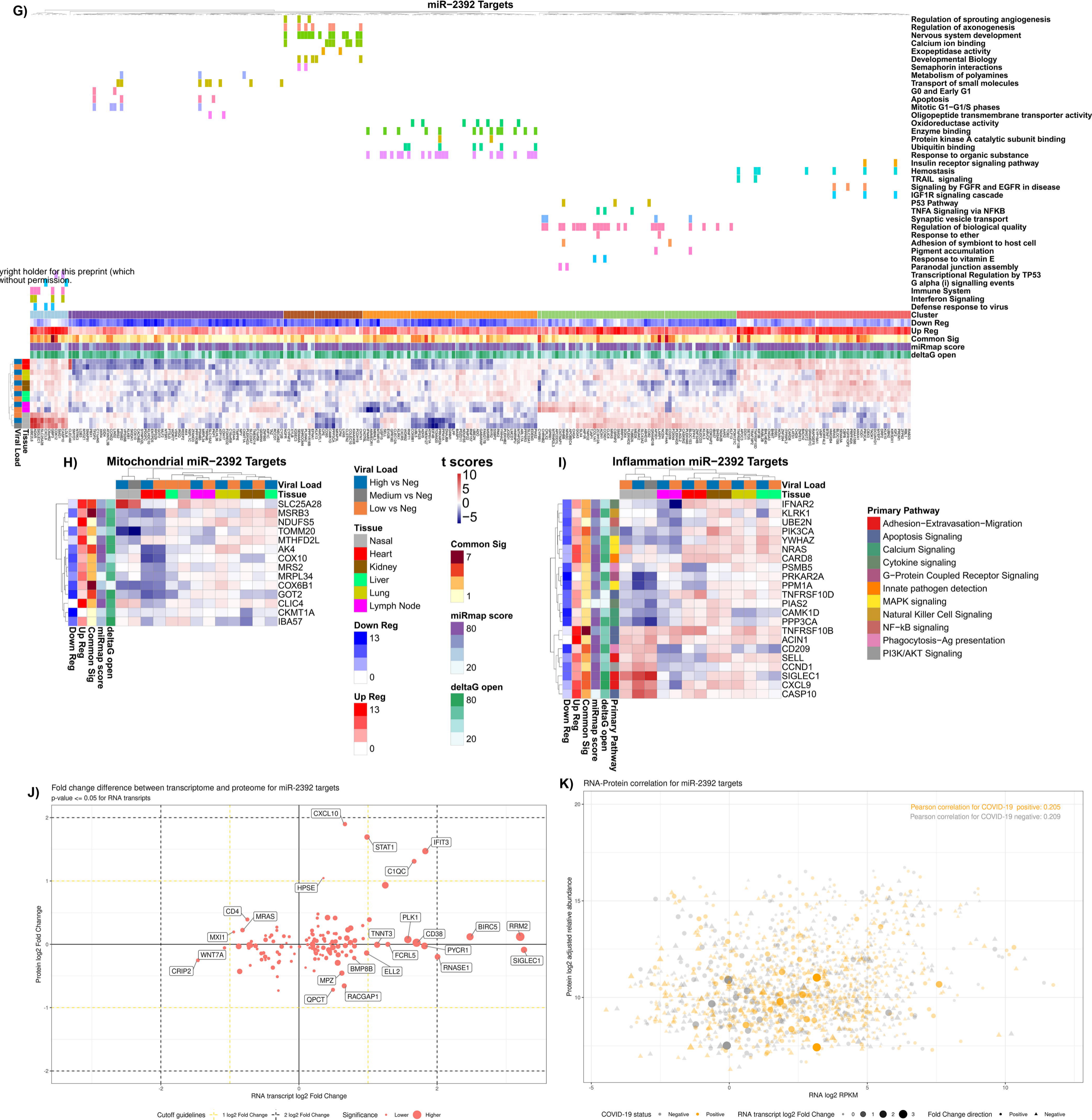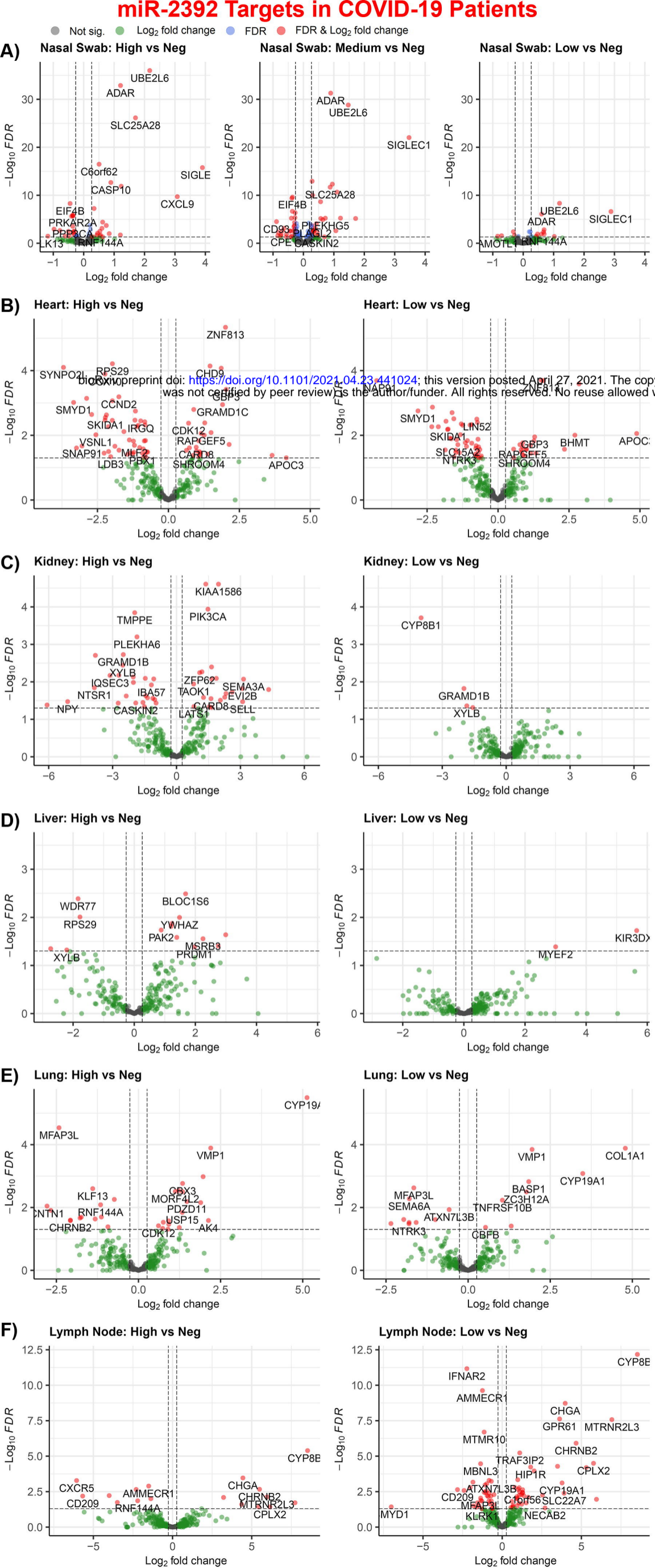
1570 Self, W.H., Tenforde, M.W., Stubblefield, W.B., Feldstein, L.R., Steingrub, J.S., Shapiro, N.I.,
1571 Ginde, A.A., Prekker, M.E., Brown, S.M., Peltan, I.D.*, et al.* (2020). Decline in SARS-CoV-2
1572 Antibodies After Mild Infection Among Frontline Health Care Personnel in a Multistate Hospital
1573 Network - 12 States, April-August 2020. MMWR Morb Mortal Wkly Rep *69*, 1762-1766.

1574 Shannon, P., Markiel, A., Ozier, O., Baliga, N.S., Wang, J.T., Ramage, D., Amin, N.,
1575 Schwikowski, B., and Ideker, T. (2003). Cytoscape: a software environment for integrated
1576 models of biomolecular interaction networks. Genome Res *13*, 2498-2504.

1577 Shu, Y., and McCauley, J. (2017). GISAID: Global initiative on sharing all influenza data - from
1578 vision to reality. Euro Surveill *22*.

1579 Singh, U., Hur, M., Dorman, K., and Wurtele, E.S. (2020). MetaOmGraph: a workbench for
1580 interactive exploratory data analysis of large expression datasets. Nucleic Acids Res *48*, e23.

1581 Singh, U., Li, J., Seetharam, A., and Wurtele, E.S. (2021). pyrpipe: a python package for RNA-
1582 Seq workflows. bioRxiv, 2020.2003.2004.925818.

1583 Sirin, D.A., and Ozcelik, F. (2021). The relationship between COVID-19 and the dental damage
1584 stage determined by radiological examination. Oral Radiol.

1585 Sirota, M., Dudley, J.T., Kim, J., Chiang, A.P., Morgan, A.A., Sweet-Cordero, A., Sage, J., and
1586 Butte, A.J. (2011). Discovery and preclinical validation of drug indications using compendia of
1587 public gene expression data. Sci Transl Med *3*, 96ra77.

1588 Srivastava, A., Malik, L., Sarkar, H., Zakeri, M., Almodaresi, F., Soneson, C., Love, M.I.,
1589 Kingsford, C., and Patro, R. (2020). Alignment and mapping methodology influence transcript
1590 abundance estimation. Genome Biol *21*, 239.

1591 Su, M., Chen, Y., Qi, S., Shi, D., Feng, L., and Sun, D. (2020). A Mini-Review on Cell Cycle
1592 Regulation of Coronavirus Infection. Front Vet Sci *7*, 586826.

1593 Subramanian, A., Tamayo, P., Mootha, V.K., Mukherjee, S., Ebert, B.L., Gillette, M.A.,
1594 Paulovich, A., Pomeroy, S.L., Golub, T.R., Lander, E.S.*, et al.* (2005). Gene set enrichment
1595 analysis: a knowledge-based approach for interpreting genome-wide expression profiles. Proc
1596 Natl Acad Sci U S A *102*, 15545-15550.

1597 Sullivan, K.D., Galbraith, M.D., Kinning, K.T., Bartsch, K., Levinsky, N., Araya, P., Smith,
1598 K.P., Granrath, R.E., Shaw, J.R., Baxter, R.*, et al.* (2021). The COVIDome Explorer Researcher
1599 Portal. medRxiv.

1600 Tang, H., Gao, Y., Li, Z., Miao, Y., Huang, Z., Liu, X., Xie, L., Li, H., Wen, W., Zheng, Y.*, et*
1601 *al.* (2020). The noncoding and coding transcriptional landscape of the peripheral immune
1602 response in patients with COVID-19. Clin Transl Med *10*, e200.

1603 Teodori, L., Sestili, P., Madiai, V., Coppari, S., Fraternale, D., Rocchi, M.B.L., Ramakrishna, S.,
1604 and Albertini, M.C. (2020). MicroRNAs Bioinformatics Analyses Identifying HDAC Pathway as
1605 a Putative Target for Existing Anti-COVID-19 Therapeutics. Front Pharmacol *11*, 582003.

1606 Thibault, P.A., Huys, A., Amador-Canizares, Y., Gailius, J.E., Pinel, D.E., and Wilson, J.A.
1607 (2015). Regulation of Hepatitis C Virus Genome Replication by Xrn1 and MicroRNA-122
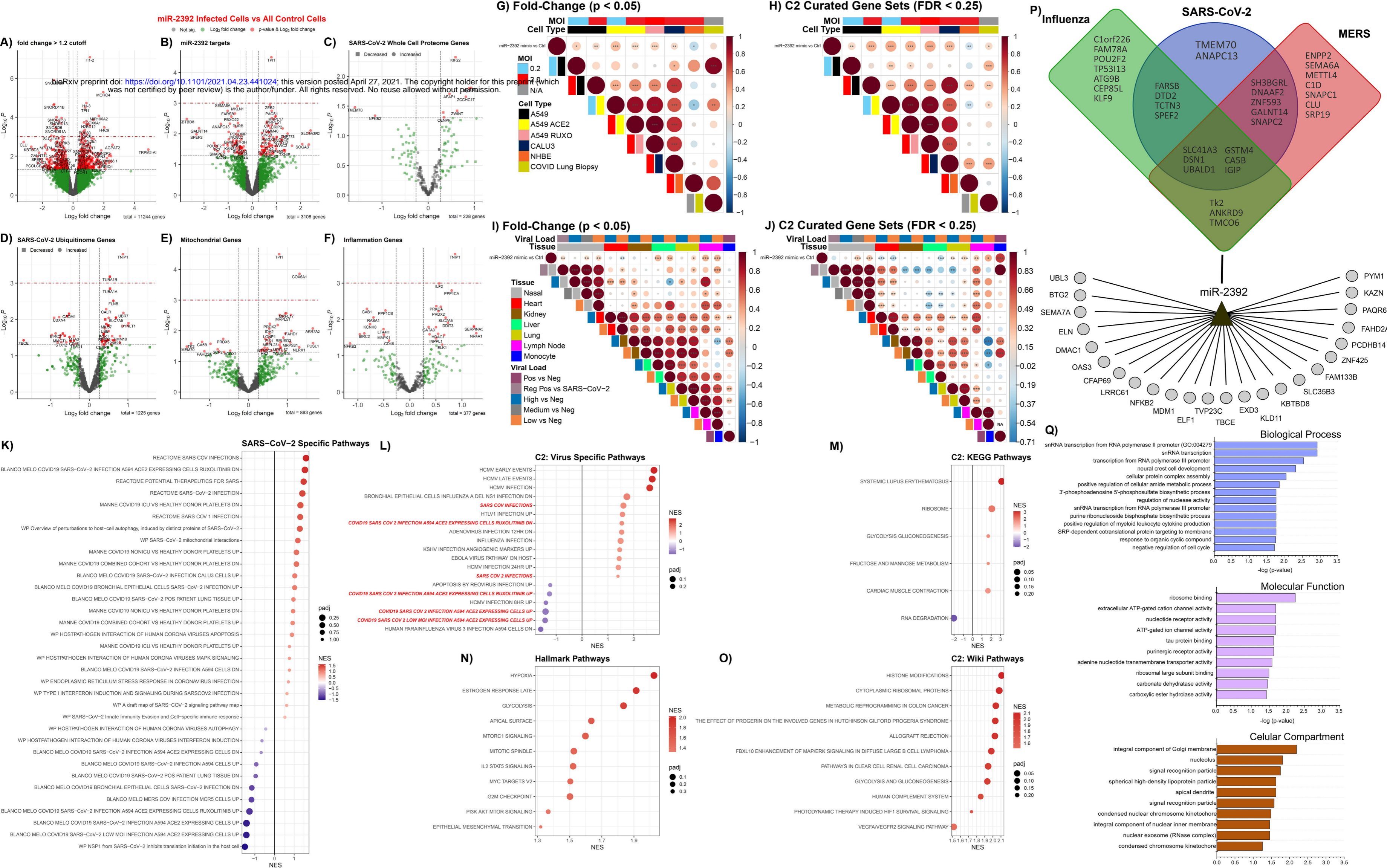1608 Binding to Individual Sites in the 5' Untranslated Region. J Virol *89*, 6294-6311.

1609 Tribolet, L., Kerr, E., Cowled, C., Bean, A.G.D., Stewart, C.R., Dearnley, M., and Farr, R.J.
1610 (2020). MicroRNA Biomarkers for Infectious Diseases: From Basic Research to Biosensing.
1611 Front Microbiol *11*, 1197.

1612 Trobaugh, D.W., and Klimstra, W.B. (2017). MicroRNA Regulation of RNA Virus Replication
1613 and Pathogenesis. Trends Mol Med *23*, 80-93.

1614 V'Kovski, P., Kratzel, A., Steiner, S., Stalder, H., and Thiel, V. (2021). Coronavirus biology and
1615 replication: implications for SARS-CoV-2. Nat Rev Microbiol *19*, 155-170.

1616 van der Ree, M.H., de Vree, J.M., Stelma, F., Willemse, S., van der Valk, M., Rietdijk, S.,
1617 Molenkamp, R., Schinkel, J., van Nuenen, A.C., Beuers, U.*, et al.* (2017). Safety, tolerability,
1618 and antiviral effect of RG-101 in patients with chronic hepatitis C: a phase 1B, double-blind,
1619 randomised controlled trial. Lancet *389*, 709-717.

1620 Vejnar, C.E., and Zdobnov, E.M. (2012). MiRmap: comprehensive prediction of microRNA
1621 target repression strength. Nucleic Acids Res *40*, 11673-11683.

1622 Wallace, D.C. (2018). Mitochondrial genetic medicine. Nat Genet *50*, 1642-1649.

1623 Walsh-Messinger, J., Manis, H., Vrabec, A., Sizemore, J., Bishof, K., Debidda, M., Malaspina,
1624 D., and Greenspan, N. (2020). The Kids Are Not Alright: A Preliminary Report of Post-COVID
1625 Syndrome in University Students. medRxiv.

1626 West, A.P., Khoury-Hanold, W., Staron, M., Tal, M.C., Pineda, C.M., Lang, S.M., Bestwick, M.,
1627 Duguay, B.A., Raimundo, N., MacDuff, D.A.*, et al.* (2015). Mitochondrial DNA stress primes
1628 the antiviral innate immune response. Nature *520*, 553-557.

1629 West, A.P., and Shadel, G.S. (2017). Mitochondrial DNA in innate immune responses and
1630 inflammatory pathology. Nat Rev Immunol *17*, 363-375.

1631 Wickham, H. (2016). ggplot2: Elegant Graphics for Data Analysis (Springer-Verlag New York).

1632 Widiasta, A., Sribudiani, Y., Nugrahapraja, H., Hilmanto, D., Sekarwana, N., and Rachmadi, D.
1633 (2020). Potential role of ACE2-related microRNAs in COVID-19-associated nephropathy.
1634 Noncoding RNA Res *5*, 153-166.

1635 Yang, J., Li, C., Li, H., and E, C. (2019). LncRNA CACNA1G-AS1 facilitates hepatocellular
1636 carcinoma progression through the miR-2392/C1orf61 pathway. J Cell Physiol *234*, 18415-
1637 18422.

1638 Yang, S., Pei, Y., Li, X., Zhao, S., Zhu, M., and Zhao, A. (2016). miR-124 attenuates Japanese
1639 encephalitis virus replication by targeting DNM2. Virol J *13*, 105.

1640 Younis, J.S., Abassi, Z., and Skorecki, K. (2020). Is there an impact of the COVID-19 pandemic
1641 on male fertility? The ACE2 connection. Am J Physiol Endocrinol Metab *318*, E878-E880.

1642 Zamani, B., Moeini Taba, S.M., and Shayestehpour, M. (2021). Systemic lupus erythematosus
1643 manifestation following COVID-19: a case report. J Med Case Rep *15*, 29.

1644 Zhong, Z., Liang, S., Sanchez-Lopez, E., He, F., Shalapour, S., Lin, X.J., Wong, J., Ding, S.,
1645 Seki, E., Schnabl, B.*, et al.* (2018). New mitochondrial DNA synthesis enables NLRP3
1646 inflammasome activation. Nature *560*, 198-203.

1647 Zhu, N., Zhang, D., Wang, W., Li, X., Yang, B., Song, J., Zhao, X., Huang, B., Shi, W., Lu, R.*,
1648 et al.* (2020). A Novel Coronavirus from Patients with Pneumonia in China, 2019. N Engl J Med
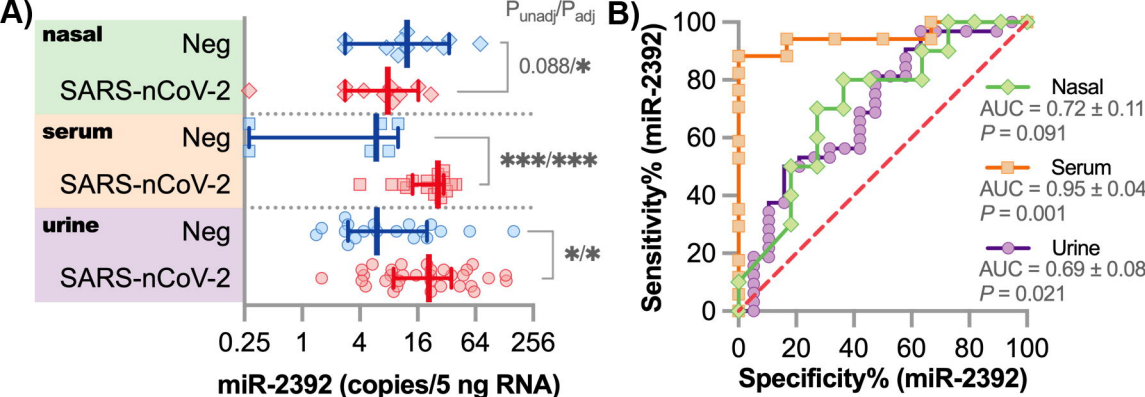1649 *382*, 727-733.

Abdelrahman, Z., Liu, Q., Jiang, S., Li, M., Sun, Q., Zhang, Y., and Wang, X. (2021). Evaluation of the Current Therapeutic Approaches for COVID-19: A Systematic Review and a Meta-analysis. Front Pharmacol *12*, 607408.

Alamdari, D.H., Moghaddam, A.B., Amini, S., Keramati, M.R., Zarmehri, A.M., Alamdari, A.H., Damsaz, M., Banpour, H., Yarahmadi, A., and Koliakos, G. (2020). Application of methylene blue -vitamin C -N-acetyl cysteine for treatment of critically ill COVID-19 patients, report of a phase-I clinical trial. Eur J Pharmacol *885*, 173494.

Ardestani, A., and Azizi, Z. (2021). Targeting glucose metabolism for treatment of COVID-19. Signal Transduct Target Ther *6*, 112.

Bojkova, D., Klann, K., Koch, B., Widera, M., Krause, D., Ciesek, S., Cinatl, J., and Munch, C. (2020). Proteomics of SARS-CoV-2-infected host cells reveals therapy targets. Nature *583*, 469-472.

Codo, A.C., Davanzo, G.G., Monteiro, L.B., de Souza, G.F., Muraro, S.P., Virgilio-da-Silva, J.V., Prodonoff, J.S., Carregari, V.C., de Biagi Junior, C.A.O., Crunfli, F.*, et al.* (2020). Elevated Glucose Levels Favor SARS-CoV-2 Infection and Monocyte Response through a HIF-1alpha/Glycolysis-Dependent Axis. Cell Metab *32*, 437-446 e435.

Mishra, P.K., Tandon, R., and Byrareddy, S.N. (2020). Diabetes and COVID-19 risk: an miRNA perspective. Am J Physiol Heart Circ Physiol *319*, H604-H609.

Nersisyan, S., Engibaryan, N., Gorbonos, A., Kirdey, K., Makhonin, A., and Tonevitsky, A. (2020). Potential role of cellular miRNAs in coronavirus-host interplay. PeerJ *8*, e9994.

Overbey, E.G., Saravia-Butler, A.M., Zhang, Z., Rathi, K.S., Fogle, H., da Silveira, W.A., Barker, R.J., Bass, J.J., Beheshti, A., Berrios, D.C.*, et al.* (2021). NASA GeneLab RNA-seq consensus pipeline: standardized processing of short-read RNA-seq data. iScience *24*.

Portincasa, P., Krawczyk, M., Machill, A., Lammert, F., and Di Ciaula, A. (2020). Hepatic consequences of COVID-19 infection. Lapping or biting? Eur J Intern Med *77*, 18-24.

Ren, L., Zhang, R., Rao, J., Xiao, Y., Zhang, Z., Yang, B., Cao, D., Zhong, H., Ning, P., Shang, Y.*, et al.* (2018). Transcriptionally Active Lung Microbiome and Its Association with Bacterial Biomass and Host Inflammatory Status. mSystems *3*.

Ritchie, M.E., Phipson, B., Wu, D., Hu, Y., Law, C.W., Shi, W., and Smyth, G.K. (2015). limma powers differential expression analyses for RNA-sequencing and microarray studies. Nucleic Acids Res *43*, e47.

Sacar Demirci, M.D., and Adan, A. (2020). Computational analysis of microRNA-mediated interactions in SARS-CoV-2 infection. PeerJ *8*, e9369.

Sardar, R., Satish, D., and Gupta, D. (2020). Identification of Novel SARS-CoV-2 Drug Targets by Host MicroRNAs and Transcription Factors Co-regulatory Interaction Network Analysis. Front Genet *11*, 571274.

Shen, Z., Xiao, Y., Kang, L., Ma, W., Shi, L., Zhang, L., Zhou, Z., Yang, J., Zhong, J., Yang, D.*, et al.* (2020). Genomic Diversity of Severe Acute Respiratory Syndrome-Coronavirus 2 in Patients With Coronavirus Disease 2019. Clin Infect Dis *71*, 713-720.

1689   Stukalov, A., Girault, V., Grass, V., Karayel, O., Bergant, V., Urban, C., Haas, D.A., Huang, Y.,
1690   Oubraham, L., Wang, A.*, et al.* (2021). Multilevel proteomics reveals host perturbations by
1691   SARS-CoV-2 and SARS-CoV. bioRxiv, 2020.2006.2017.156455.

1692   Teodori, L., Sestili, P., Madiai, V., Coppari, S., Fraternale, D., Rocchi, M.B.L., Ramakrishna, S.,
1693   and Albertini, M.C. (2020). MicroRNAs Bioinformatics Analyses Identifying HDAC Pathway as
1694   a Putative Target for Existing Anti-COVID-19 Therapeutics. Front Pharmacol *11*, 582003.

1695   Widiasta, A., Sribudiani, Y., Nugrahapraja, H., Hilmanto, D., Sekarwana, N., and Rachmadi, D.
1696   (2020). Potential role of ACE2-related microRNAs in COVID-19-associated nephropathy.
1697   Noncoding RNA Res *5*, 153-166.

1698   Zhang, S., Amahong, K., Sun, X., Lian, X., Liu, J., Sun, H., Lou, Y., Zhu, F., and Qiu, Y. (2021).
1699   The miRNA: a small but powerful RNA for COVID-19. Brief Bioinform *22*, 1137-1149.

1700

A) Scale: 10 bases; chr14: 100,814,555, 100,814,560, 100,814,565 (hg38). Tracks include Chromosome Bands Localized by FISH Mapping Clones (14q32.2), GC Percent in 5-Base Windows, GENCODE v32 Comprehensive Transcript Set (MEG3, MIR2392), CRISPR/Cas9 -NGG Targets, lincRNA and TUCP transcripts, C/D and H/ACA Box snoRNAs, scaRNAs, and microRNAs from snoRNABase and miRBase (hsa-mir-2392), Gene Expression in 54 tissues from GTEx RNA-seq of 17382 samples, 948 donors (V8, Aug 2019), Tissue-Specific microRNA Expression from Two Individuals, 100 vertebrates Basewise Conservation by PhyloP, 100 vertebrates Conserved Elements, Multiz Alignments of 100 Vertebrates, and Simple Nucleotide Polymorphisms (dbSNP 151).

B) Gene expression for MEG3 (ENSG00000214548.14)

C) Visualizing potential binding sites for miRNA-2392

3 top hits from miRNA-2392 to NC_045512.2 reference genome:

NC_045512.2:2130-2149 (NSP2, ORF1ab)
Query: 3' gtggaGAGTGGGGGTAGGAt 5'
              ||||| ||:|||
Ref: 5' aaaaaCTCAAACCCGTCCTt 3'
Energy: -23.900000 kCal/Mol

NC_045512.2:7153-7172 (NSP3, ORF1ab)
Query: 3' gtGGGAGAGTGGGGGTAGGAt 5'
             :|:| || |||:|||||
Ref: 5' ttCTTTAGACACCTATCCTt 3'
Energy: -18.320000 kCal/Mol

NC_045512.2:26326-26346 (E gene)
Query: 3' gtggAGATGG-GGGTAGGAt 5'
             :| ||| : ||||||
Ref: 5' ctagTTACACTAGCCATCCTt 3'
Energy: -17.820000 kCal/Mol

miR-2392 Targets in COVID-19 Patients

A)

nasal
- Neg
- SARS-nCoV-2

serum
- Neg
- SARS-nCoV-2

urine
- Neg
- SARS-nCoV-2

P_{unadj}/P_{adj}
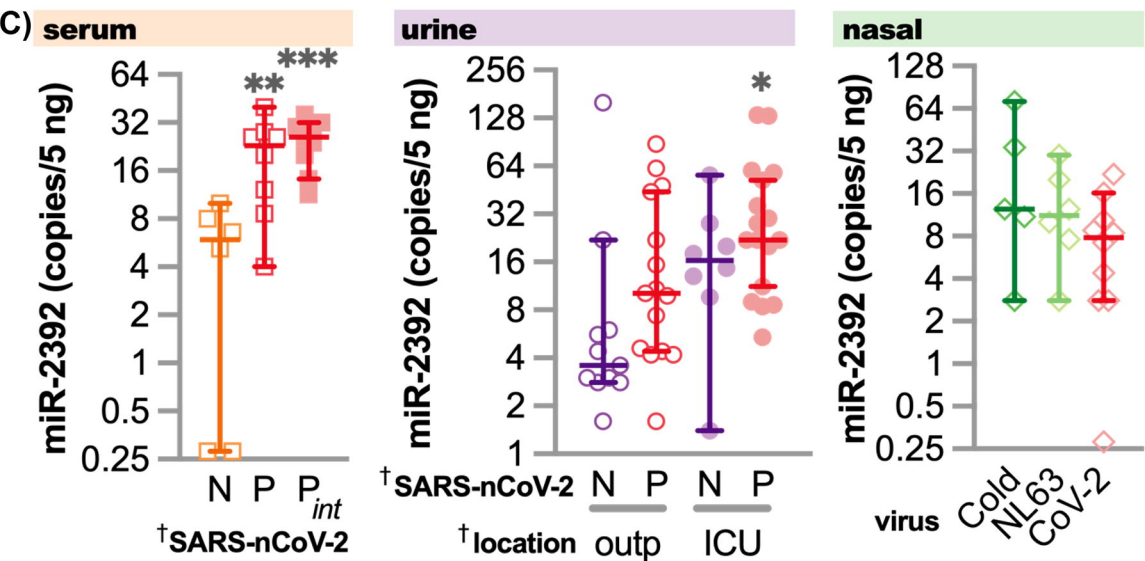
0.088/*

/

/

miR-2392 (copies/5 ng RNA)

unadjusted = t-test on SARS (on log transformed values)
adjusted = mixed model corrected for age and sex (single terms)
*, **, *** = p < 0.05, 0.01, 0.001

B)

Sensitivity% (miR-2392)
Specificity% (miR-2392)

Nasal
AUC = 0.72 ± 0.11
P = 0.091

Serum
AUC = 0.95 ± 0.04
P = 0.001

Urine
AUC = 0.69 ± 0.08
P = 0.021

AUC = area under the curve

C)

serum

miR-2392 (copies/5 ng)

** ***

N   P P_{int}

†SARS-nCoV-2

urine

miR-2392 (copies/5 ng)

*

†SARS-nCoV-2   N   P   N   P

†location   outp   ICU

nasal

miR-2392 (copies/5 ng)

Cold   NL63   CoV-2

virus

nasal and serum = ANOVA on log values
urine = 2-way ANOVA on log values
†, †† = p < 0.05, 0.01 from ANOVA
*, **, *** = p < 0.05, 0.01, 0.001 from Dunnet's post-test compared to Negative

A) miR-2392 Predicted Diseases